



Interstellar Polarization Survey. III. Relation between Optical Polarization and Reddening in the General Interstellar Medium

Y. Angarita¹, M. J. F. Versteeg¹, M. Haverkorn¹, C. V. Rodrigues², A. M. Magalhães³, R. Santos-Lima³, and Koji S. Kawabata⁴

¹ Department of Astrophysics/IMAPP, Radboud University, PO Box 9010, 6500 GL Nijmegen, The Netherlands; y.angarita@astro.ru.nl

² Divisão de Astrofísica, Instituto Nacional de Pesquisas Espaciais (INPE/MCTI), Av. dos Astronautas, 1758, São José dos Campos, SP, Brazil

³ Instituto de Astronomia, Geofísica e Ciências Atmosféricas, Universidade de São Paulo, R. do Matão, 1226, São Paulo, SP 05508-090, Brazil

⁴ Hiroshima Astrophysical Science Center, Hiroshima University, Kagamiyama, Higashi-Hiroshima, Hiroshima, 739-8526, Japan

Received 2023 March 17; revised 2023 June 5; accepted 2023 June 5; published 2023 June 28

Abstract

Optical starlight can be partially polarized while propagating through the dusty, magnetized interstellar medium (ISM). The polarization efficiency describes the polarization intensity fraction per reddening unit, $P_V/E(B - V)$, related to the interstellar dust grains and magnetic field properties. The maximum value observed, $[P_V/E(B - V)]_{\max}$, is thus achieved under optimal polarizing conditions of the ISM. Therefore, the analysis of polarization efficiency observations across the Galaxy contributes to the study of magnetic field topology, small-scale magnetic fluctuations, grain-alignment efficiency, and composition. Infrared observations from Planck satellite have set $[P_V/E(B - V)]_{\max}$ to 13% mag⁻¹. However, recent optical polarization observations in Planck's highly polarized regions showed polarization efficiency values between 13.6% mag⁻¹ and 18.2% mag⁻¹ (depending on the extinction map used), indicating that $[P_V/E(B - V)]_{\max}$ is not well constrained yet. We used V-band polarimetry of the Interstellar Polarization Survey (consisting of $\sim 10,500$ high-quality observations distributed in 34 fields of 0.3×0.3) to accurately estimate the polarization efficiency in the ISM. We estimated the upper limit of $P_V/E(B - V)$ with the weighted 99th percentile of the field. In five regions, the polarization efficiency upper limit is above 13% mag⁻¹. Furthermore, we found $[P_V/E(B - V)]_{\max} = 15.8_{-0.9}^{+1.3}$ % mag⁻¹ using diffuse intermediate-latitude ($|b| > 7.5$) regions with apparently strong regular Galactic magnetic field in the plane-of-sky. We studied the variations of $P_V/E(B - V)$ across the sky and tested toy models of polarization efficiency with Galactic longitude that showed some correspondence with a uniform spiral magnetic field.

Unified Astronomy Thesaurus concepts: Starlight polarization (1571); Optical observation (1169); Interstellar medium (847); Interstellar magnetic fields (845); Interstellar dust (836); Interstellar dust extinction (837)

Supporting material: figure set, machine-readable table

1. Introduction

The dichroic extinction of starlight from elongated dust grains aligned with the Galactic magnetic field (GMF) causes interstellar optical linear polarization parallel to the rotation axis of the grains. The optical polarization is, therefore, tied not only to the properties of the GMF but also to the properties of the dust grains in the interstellar medium (ISM). Together, optical polarization and dust extinction are essential for studying the plane-of-sky component of the GMF at small and large scales, in addition to other properties of the ISM, such as grain alignment and composition (see, e.g., reviews of Beck & Wielebinski 2013; Andersson et al. 2015).

The ratio between V-band polarization fraction and the color excess, $P_V/E(B - V)$, is known as polarization efficiency. The distribution of $P_V/E(B - V)$ may contain relevant information about mechanisms that reduce the polarization efficiency, such as magnetohydrodynamic turbulence, which is known to permeate the different phases of the ISM (Beresnyak & Lazarian 2019). The maximum polarization efficiency, in turn, represents the highest degree of polarization possible for a given color excess, which might be achieved under optimal

polarizing conditions of the ISM, i.e., elongated grains, full grain alignment, and uniform magnetic field with lines oriented parallel to the plane-of-sky.

Serkowski et al. (1975) proposed one of the first empirical estimates of the maximum polarization efficiency as $P_V/E(B - V) \leq 9\%$ mag⁻¹, using the ratio of total to selective extinction $R_{\lambda_{\max}} = 3.0$ and the maximum polarization fraction at λ_{\max} , the wavelength of maximum polarization. Many years later, Fosalba et al. (2002) found a power law, $P_V = 3.5 E(B - V)^{0.8}$, that describes the median trend of polarization with reddening for the whole sky using the Heiles (2000) optical polarimetry database. Recently, Planck Collaboration et al. (2020) released thermal dust polarization maps and established a new indirect measurement of polarization efficiency using highly polarized regions in diffuse ISM at high latitudes. They found $P_V/E(B - V) = 13\%$ mag⁻¹, where the polarization fraction in absorption, P_V , is obtained from the correlation with the submillimeter polarization in emission and the so-called polarization ratios (Planck Collaboration Int et al. 2015). They assumed a ratio of total to selective extinction of $R_V = 3.1$ (Fitzpatrick 2004) and used the optical depth and extinction relation $\tau_V = A_V/1.086$. Furthermore, Panopoulou et al. (2019) did an optical polarimetric analysis (in the R band) in some highly polarized regions of Planck maps. They found $P_V/E(B - V)$ values between 13.6% mag⁻¹ and 18.2% mag⁻¹ depending on the extinction map used and proposed the former as the lower limit of the maximum polarization efficiency. The

determination of the true maximum value is, therefore, highly dependent on the systematic uncertainties of the dust map chosen. There is then a large uncertainty in the maximum polarization efficiency value for the general ISM.

Optical starlight polarization allows for the study of ISM properties at a higher spatial resolution (parsec and subparsec scales) compared to Planck’s submillimeter observations (with $\sim 5'$ resolution at intermediate latitude; Planck Collaboration Int et al. 2015). The Interstellar Polarization Survey (IPS; Magalhães et al. 2005; 2023, in preparation), is a pilot survey, already completed, that illustrates the potential of future high-resolution optical polarimetry surveys such as SOUTHPOL (Magalhães et al. 2012) and PASIPHAË (Tassis et al. 2018). In combination with accurate distances to the stars from Gaia Collaboration et al. (2021, hereafter *Gaia*–EDR3), the IPS catalog in the general ISM, IPS-GI (Versteeg et al. 2023), will let us reconstruct the information from the magnetic field and absorption structures along the line of sight (LOS).

We use high-quality polarimetry and photometry measurements of $\sim 10,500$ stars of the IPS-GI catalog (Versteeg et al. 2023), distributed in 34 high spatial density regions, to study the GMF and dust grain properties through the $P_V/E(B-V)$ relation under the same ISM conditions in each field observed. Contrarily, Fosalba et al. (2002) and Planck Collaboration et al. (2020) calculated the maximum polarization efficiency using many different LOSs across the entire sky. The observations and data are described in detail in Section 2. In Section 3, we describe the V -band extinction of Anders et al. (2022, hereafter *Anders22*), used to obtain the reddening and the polarization efficiency. We also compare *Anders22* reddening with other measurements available. In Section 4 we show the relation between the degree of polarization and the reddening under different ISM conditions, as well as the method to calculate its upper envelope. Our results on the $P_V/E(B-V)$ upper-limit calculation are presented in Section 5. Furthermore, we discuss the variations of the polarization efficiency observed across the Southern sky, the possible explanation with toy models, the dependency on the dust map used, and the correlation with the dispersion of polarization angle in Section 6. Finally, we summarize our findings in Section 7.

2. Polarimetric Observations and Data

In this section, we describe the data acquisition and reduction, the cross-match with auxiliary databases, and the selection of high-quality objects to study polarization efficiency.

2.1. Interstellar Polarization Survey

One of the scientific aims of the IPS is to improve our knowledge of the magnetic field structure in the general ISM in relation to its dust properties (Magalhães et al. 2005). For that purpose, different types of sources such as open clusters, nearby dark clouds, and the general ISM were observed between 2000 and 2003 with the IAGPOL polarimeter developed at the *Instituto de Astronomia, Geofísica e Ciências Atmosféricas* of the *Universidade de São Paulo* (IAG-USP), Brazil (Magalhães et al. 2005). This optical/NIR imaging polarimeter (see Magalhães et al. 1996) is equipped with a Savart prism and a rotating half-wave plate and is mounted ahead of a CCD detector. The assembly was installed onto the Cassegrain focus of the IAG Boller & Chivens 61 cm telescope

at the Observatório do Pico dos Dias (OPD) in Brazil. The Savart prism forms the extraordinary and ordinary beams, i.e., two perpendicularly polarized images of every source in the field of view. Such a dual-beam polarimeter allows us to cancel out the sky polarization through the superposition of the extraordinary and ordinary images. Additionally, the differential photometry technique used allows for observations even in nonphotometric conditions. Further information about the IPS project, the polarimetry, and observations can be found in Magalhães et al. (2005; 2023, in preparation; Versteeg et al. 2023).

2.2. General ISM Data

Our research focuses on the study of the general ISM fields observed in the IPS project (IPS-GI). A new photometric and polarimetric catalog with precise measurements of the degree of polarization (P), polarization angle (θ), and magnitudes in the V band is presented in detail by Versteeg et al. (2023). The new stellar catalog contains data from 38 fields of approximately 0.3×0.3 in size, carefully chosen in different locations near and within the Galactic disk in the Southern sky.

2.3. Data Reduction

Polarimetric and photometric information was obtained with the reduction pipeline SOLVEPOL developed by Ramírez et al. (2017). The algorithm, written in IDL, calculates the Stokes parameters Q and U from the modulation of the intensity in terms of the ordinary and extraordinary fluxes. In this process, Q and U are normalized by the intensity, i.e., the I Stokes parameter. The degree of linear polarization and polarization angle are calculated as:

$$P = \sqrt{Q^2 + U^2}, \quad (1)$$

$$\theta = \frac{1}{2} \tan^{-1} \frac{U}{Q}. \quad (2)$$

Following Magalhães et al. (1984) and Naghizadeh-Khouei & Clarke (1993), $\sigma_U \approx \sigma_Q \approx \sigma_P$ is assumed. The uncertainties are calculated as in Ramírez et al. (2017):

$$\sigma_P = \frac{1}{\sqrt{\mu - 2}} \sqrt{\frac{2}{\mu} \sum_i z_i^2 - Q^2 - U^2}, \quad (3)$$

$$\sigma_\theta = 28.65 \frac{\sigma_P}{P}, \quad (4)$$

where μ is the number of positions of the half-wave plate, and z_i is the ratio between the difference and the sum of the ordinary and extraordinary beams of the i th orientation of the half-wave plate (see Ramírez et al. 2017).

The degree of polarization measured is affected by Ricean bias, especially at low signal-to-noise ratios ($P/\sigma_P \leq 3$, according to Clarke & Stewart 1986). The SOLVEPOL pipeline itself purposely does not correct for the bias. However, following Ramírez et al. (2017) recommendations, we used only high signal-to-noise measurements with $P/\sigma_P > 5$, which are not significantly affected by the bias (Simmons & Stewart 1985; also see the quality filters in Section 2.5). Furthermore, since the average instrumental polarization is 0.07% (see Versteeg et al. 2023), far below the median polarization error, there is no need to correct instrumental errors.

2.4. Auxiliary Data

We used the IPS-GI catalog (Versteeg et al. 2023) containing G -, G_{BP} -, G_{RP} -, and V -band parameters from the *Gaia*-EDR3 and *Anders22* catalogs. The latter used *Gaia*-EDR3 parallaxes and photometry to estimate accurate distances and V -band extinction of millions of stars. First, around 44,000 IPS-GI stars with photometric and polarimetric measurements in the V band were cross-matched with the *Gaia*-EDR3 database using a cone search with $3''$ and 2 mag margins in TOPCAT (Taylor 2005). Subsequently, we used *Gaia*-EDR3's *source ID* parameter of the successful matches to cross-match with the *Anders22* database. Finally, we kept approximately 36,000 stars from the original IPS-GI catalog that have measurements of distance and V -band extinction.

2.5. Quality Filters

In order to use the IPS-GI data together with known parameters from *Anders22* and *Gaia*-EDR3 databases, certain filters must be defined to ensure a high quality of the final data set and the reliability of its parameters. Below we will explain each of the quality filters in order of importance and the number of sources removed or remaining after the flagging.

2.5.1. Signal-to-noise Ratio and Polarization Uncertainty

The bias of the degree of polarization mainly depends on the signal-to-noise ratios (Clarke & Stewart 1986). The lower the signal-to-noise, the larger the polarization bias. A signal-to-noise cut of $P_V/\sigma_{P_V} > 5$ was defined through the SOLVEPOL pipeline to eliminate low signal-to-noise measurements. This filter discards $\sim 46\%$ of the initial sample, resulting in $\sim 16,800$ sources for which the degree of polarization is still biased. However, Versteeg et al. (2023) demonstrated that the difference between the biased and debiased polarization fraction after filtering is of the order of $10^{-3}\%$. Consequently, we see no need to debias the degree of polarization of the filtered sample.

We observed an increase in the degree of polarization and its uncertainty with higher V magnitudes in the IPS-GI data. Although this is expected, an anomalous increasing noise with magnitude may originate in the data reduction process. Ramírez et al. (2017) reported that the procedure followed by IDL within the SOLVEPOL pipeline to calculate the sky flux can yield a different estimation of the total flux in comparison with other methods (e.g., IRAF; Tody 1986, 1993). The difference in flux propagates through the pipeline affecting the final polarization and its uncertainty, especially for low-count objects, which are often the faintest stars. Therefore, we only included stars with $\sigma_{P_V} \leq 0.8\%$ to avoid untrustworthy and noisy high-polarization values, reducing the sample size to $\sim 15,700$ stars.

2.5.2. Fidelity

The *fidelity* is a metric defined by Rybizki et al. (2022) using neural networks and all astrometric columns available from *Gaia*-EDR3. It summarizes the goodness of the astrometric solutions. Following Rybizki et al. (2022) and *Anders22* recommendations, we use stars with *fidelity* > 0.5 . This leaves us with $\sim 14,700$ stars.

2.5.3. Color Excess Factor

The corrected $G_{BP} - G_{RP}$ flux excess factor, C^* , is a correction applied to the ratio between the total $G_{BP} - G_{RP}$ flux and the G -band flux. It identifies inconsistencies between G , G_{BP} , and G_{RP} photometry due to background flux from different sources (Riello et al. 2021). The *color excess factor* is defined as $|C^*|/\sigma_{C^*}$, where σ_{C^*} is a function of G -magnitude described in Equation (18) from Riello et al. (2021). It might reveal some objects whose photometry measurements are complicated, including variable stars, extended sources, and multiple stars. Still, the *color excess factor* is not intended to identify all of them properly as it cannot establish the difference between data affected by processing problems and variable sources. *Anders22* suggested to use $|C^*|/\sigma_{C^*} < 5$; with this limit, we end up with $\sim 14,300$ sources.

2.5.4. Output Flag

Anders22 database includes the SH_OUTFLAG, an output parameter with four digits that denote the fidelity of the algorithm in calculating the output parameters. The first digit represents the low number of consistent models, a digit different from “0” means that the number of stellar models is too low (< 30) to be trusted. The second digit is a flag for significantly negative extinctions in which the accepted values are marked also with a “0.” The third and fourth digits are for very large and very small uncertainties, respectively; in all parameters, a “0” digit in both cases means acceptable parameters. We require a data set with the best quality possible by choosing stars with SH_OUTFLAG = 0000, leaving a remaining $\sim 11,500$ stars after this step.

2.5.5. Negative Extinctions

The Bayesian nature of the *Anders22* extinction, A_V , causes some sources to end up with negative values. As mentioned above, *Anders22* included in their SH_OUTFLAG parameter a flag for unreliable extinctions; even so, their definition rejects only negative values over 2σ , i.e., $A_{V95} < 0$. Therefore, we chose to use only positive median values of the extinction, hereafter A_{V50} , with $A_{V50} < 0$, rejecting the only remaining star with negative extinction.

2.5.6. Poor IPS-GI Fields

Fields that end up with very few stars (< 15) after applying all previous filters—i.e., fields *C34*, *C38*, *C44*, and *C53* (see Table 1) as defined in Versteeg et al. (2023)—are not considered since any statistical analysis carried out on these fields would be poor and unreliable. We reject here 32 stars in total.

2.5.7. Catalogs Match Duplicates

The number of detections and precision of *Gaia*-EDR3 has increased in the new release. This means that a cross-match with other catalogs becomes more difficult and less reliable in crowded regions. The cross-match process of the IPS-GI catalog with *Anders22* and *Gaia*-EDR3 databases returned multiple matches for some stars. Despite having used the V -band magnitude as a second matching criterion (see Versteeg et al. 2023, for more details), it is difficult to obtain a unique reliable match for the duplicates. An identifier was given in the column *GroupSize* to those groups of stars with multiple

Table 1
Polarization Efficiency Upper-limit Statistics per IPS-GI Field

Field	No. Stars	$\langle l \rangle$	$\langle b \rangle$	99th	Weighted 99th	84th	16th	G19 W-99th	G19 84th	G19 16th	M06 W-99th	M06 Std _{err} W-99th	PC16 W-99th	PC16 Std _{err} W-99th
(1)	(2)	(3)	(4)	(5)	(6)	(7)	(8)	(9)	(10)	(11)	(12)	(13)	(14)	(15)
C0	397	327.57	-0.83	16.1	10.9	13.1	10.0	10.16	0.21
C1	545	330.42	4.59	13.7	10.0	10.8	9.4	8.17	0.04
C2	589	359.34	13.47	20.0	14.9	17.4	13.9	14.7	16.6	13.9	17.01	0.23
C3	449	339.49	-0.42	16.4	9.1	10.6	8.2	9.03	0.08
C4	507	18.63	-4.46	9.8	8.9	9.6	8.4	9.3	10.3	9.0	10.34	0.29
C5	421	25.06	-0.74	6.6	5.7	6.4	5.4	6.2	6.8	5.7	5.41	0.12
C6	210	298.61	0.64	15.3	10.3	12.5	9.2	9.52	0.39
C7	340	41.68	3.39	7.9	6.4	7.7	5.8	6.8	8.1	6.1	5.45	0.05
C11	946	307.53	1.33	17.8	11.3	13.0	10.4	6.90	0.22
C12	881	331.04	-4.70	19.2	13.1	15.7	12.3	10.54	0.19
C13	287	333.24	3.75	14.2	9.9	11.9	9.4	10.49	0.22
C14	622	312.87	5.48	18.4	13.2	15.5	12.6	27.61	0.90
C15	458	304.71	-0.17	12.3	7.5	8.9	7.0	4.64	0.07
C16	561	301.97	-8.77	19.7	15.8	17.1	14.8	12.73	0.12
C30	37	222.54	-1.63	18.3	6.0	8.0	4.9	7.2	8.5	5.8
C35	144	271.45	-1.07	14.2	10.5	11.7	9.7	12.89	0.28
C36	191	343.29	11.97	19.1	10.0	11.9	8.8	14.50	0.66
C37	539	331.16	7.62	20.2	14.9	17.2	13.8	16.46	0.15
C39	309	303.07	1.63	17.7	9.5	11.8	8.7	7.43	0.15
C40	264	302.16	-1.21	11.3	7.9	9.1	7.2	7.11	0.16
C41	116	257.34	-0.48	10.2	7.4	8.6	6.6
C42	87	245.48	-0.11	43.5	11.0	14.9	8.5	13.3	18.8	10.8
C43	70	273.17	-0.82	19.9	10.1	13.3	8.6	14.35	1.97
C45	97	21.81	0.71	5.6	4.5	5.3	4.2	4.7	5.5	4.2	5.20	0.22
C46	36	44.21	2.66	6.1	4.8	5.3	4.3	4.8	5.3	4.5	5.61	0.54
C47	240	320.49	-1.23	15.4	11.6	12.8	10.9	9.53	0.07
C50	255	20.27	1.04	9.0	6.3	6.7	5.9	6.0	7.0	5.7	5.73	0.26
C52	177	318.76	2.78	15.1	9.3	11.6	7.7	7.78	0.30
C54	137	305.17	1.31	13.1	9.2	10.6	8.4	5.70	0.53
C55	278	15.15	1.68	10.2	6.3	7.8	5.7	6.2	7.5	5.6	8.06	0.34
C56	55	14.97	-0.96	20.5	6.8	11.1	5.8	9.3	16.6	6.8	9.30	1.75
C57	343	40.59	4.14	6.7	5.9	6.4	5.7	5.8	6.9	5.3	6.08	0.18
C58	193	351.32	0.60	8.5	5.6	6.4	5.2	-	6.59	0.29
C61	292	0.48	2.19	14.8	11.4	12.5	11.0	11.6	12.0	11.2	12.31	0.49

Note. Columns: (1) Field name; (2) Total number of high-quality stars; (3) and (4) Mean Galactic longitude and latitude of the IPS-GI field in degrees; (5) nonweighted $P_V/E(B - V)$ 99th percentile; (6), (7), and (8) The 50th, 84th, and 16th percentiles of the weighted $[P_V/E(B - V)]_{99th}$ distribution; (9), (10), and (11) The 50th, 84th, and 16th percentiles of the weighted $[P_V/E(B - V)]_{G19-99th}$ distribution using G19 reddening; (12) and (13) The median and standard error of the weighted $[P_V/E(B - V)]_{M06-99th}$ distribution using M06 reddening; (14) and (15) The median and standard error of the weighted $[P_V/E(B - V)]_{PC16-99th}$ distribution using PC16 reddening. All $P_V/E(B - V)$ values have units of [% mag⁻¹].

matches. We decided not to consider stars with more than one match. This leaves us with $\sim 10,500$ high-quality stars, spread in 34 IPS-GI fields, that make up our final data set.

2.6. Variability of the IPS-GI Sources

Intrinsic polarization originating in the environment around variable sources, e.g., due to the scattering of radiation from circumstellar dust, may contaminate our sample with information that does not represent the general ISM. Knowing the stellar classification of the IPS-GI stars would help to assess their variability and whether they could have intrinsic polarization. Unfortunately, we do not know the exact stellar type or variability status of all IPS-GI sources; even if we naively look at Gaia's H-R diagram, it would only give us a rough stellar classification.

One solution to identify variable stars within the IPS-GI sample is to cross-match our catalog with variable stars databases. We considered ASAS-SN (Jayasinghe et al.

2018, 2019a, 2019b, 2020), ATLAS-VAR (Heinze et al. 2018), and the Gaia-DR3 variable stars catalog (Eyer et al. 2022). We identified 923 variable stars inside our data set, of which 294 passed all quality filters (Section 2.5). The variable stars in IPS-GI did not show unusual values in their polarimetry properties (see, e.g., Figure A1, left). They are therefore kept in our analysis while acknowledging their existence. The details about the IPS-GI variable stars are in Appendix A.1.

3. Reddening

To calculate the polarization to reddening ratio, we need to estimate the reddening, $E(B - V)$, of the IPS-GI sources and its uncertainty. We describe and compare the different dust maps considered in the following sections. We also justify our choice of Anders22's all-sky database, which includes multiwavelength photometry, distance, and optical extinction, among other parameters, for millions of stars.

3.1. Dust Maps Considered

The most widely used interstellar dust tracer is the extinction. However, few databases have large samples of stars with reliable measurements of V -band extinction (or reddening) and distances. Moreover, there are even fewer with information in the Southern sky—or at least in the regions observed by IPS—making it hard to find a suitable dust extinction database covering our entire data set. We considered the following dust maps queried through the Python library DUSTMAPS⁵ (Green 2018) using IPS-GI Equatorial coordinates and Anders22’s distances (for comparison reasons):

1. The dust extinction map from Marshall et al. (2006, hereafter M06) used the *Besançon* model of the Galaxy (Robin et al. 2003) and the comparison of Two Micron All Sky Survey colors (Skrutskie et al. 2006) to estimate the distances and the K -band extinction along binned beams of $15' \times 15'$. The uncertainty of the estimates is the mean absolute deviation from the median extinction in the bin. We converted the K -band extinction and its error to the V band with the relative extinction value $A_K/A_V = 0.078$ (see Table 3 from Wang & Chen 2019).
2. The Generalized Needlet Internal Linear Combination optical depth map from Planck Collaboration Int. XLVIII et al. (2016, hereafter PC16) has a resolution of $\sim 5'$ in the IPS-GI regions. We use the $E(B - V) = (1.49 \times 10^4 \text{ mag}) \tau_{353}$ convention to convert the optical depth (τ_{353} , measured at 353 GHz) to reddening with the respective observed error. The PC16 reddening is then the integrated value throughout the entire Galaxy.
3. The three-dimensional dust map of the local interstellar matter from Capitanio et al. (2017) and Lallement et al. (2019, hereafter Stilism)⁶ gives the reddening calculated by Bayesian inversion of individual reddening estimates toward 71,000 stars (see Lallement et al. 2018 and Lallement et al. 2019 for more details). The resolution near the Sun is 25 pc, and the uncertainty is the standard deviation among the nearest extinction density values within the box.
4. The Bayesian dust reddening map from Green et al. (2019, hereafter G19) has a resolution on the order of $7'$. The reddening is reported in arbitrary units. So, we follow the authors’ recommendation and use Equations (29) and (30) from G19 to convert the reddening to the V band with their closest definition to Anders22-like data (for comparison reasons). We also used the suggested filter for *reliable distance* and calculate the uncertainties from the posteriors of the reddening samples, i.e., the 84th and 16th percentiles.
5. The all-sky stellar catalog from Anders22 was created with the Bayesian algorithm STARHORSE (Queiroz et al. 2018). The algorithm uses Gaia-EDR3 parallaxes and multiband photometry (cross-matched with different surveys) to estimate the posteriors of the V -band extinctions and distances, among other parameters, of millions of stars with high accuracy and precision. Similarly to G19, the errors of the estimates are calculated from the posteriors. The resolution of Anders22’s optical

extinction is based on starlight measurements of pointlike sources, i.e., of the order of $\sim 1''$.

To convert the V -band extinction, A_V , to reddening, $E(B - V)$, of any dust map or catalog, we used the total to selective extinction ratio of $R_V = A_V/E(B - V) = 3.1$ (Savage & Mathis 1979; Fitzpatrick 2004).

3.2. Dust Map Comparison

The Anders22 stellar database has multiple advantages over others due to the characteristics of our data set and the precision of their estimates. For instance, G19 and Stilism used parallaxes from Gaia Collaboration et al. (2018, Gaia-DR2), while Anders22 used more precise measurements from Gaia-EDR3, making their new results more accurate. G19 lacks information in a large portion of the Southern sky, including many of the IPS-GI regions. However, G19 is one of the dust maps used by Anders22 to calculate their extinction prior. Therefore, they should be very consistent. Stilism and M06 have reliable measurements only up to ~ 2 – 3 kpc due to the resolution and characteristics of their methods. M06 only covers the sky at $-10^\circ \geq b \geq 10^\circ$. Hence, intermediate Galactic latitude IPS-GI fields ($|b| > 10^\circ$) are missing in M06. In addition, the semiempirical nature of M06’s method makes the results largely dependent on the model parameters. Anders22, on the other hand, covered the entire sky and calculated accurate distances up to above 3 kpc. Finally, PC16’s sub-millimeter observations probe the thermal dust emission of the pathlength throughout the Galaxy, not only up to the stellar distance as Anders22. Moreover, the small angular size of the IPS-GI fields challenges the PC16 map resolution, i.e., many sources are assigned equal $E(B - V)$ measurement from a single pixel losing information from small and dense dust structures. Hence, for completeness, we only compare and analyze PC16 reddening in intermediate-latitude fields (C2, C16, C36, and C37; see Table 1), where the LOSs for IPS-GI and PC16 are assumed to be comparable.

We computed the systematic difference between the reddening of G19, M06, and PC16 with the median value of Anders22 reddening, $E(B - V)_{A22}$ (see Figure 1). The error bars in Figure 1 result from the propagation of errors from the measurements. We decided not to consider the Stilism map for further analysis since the difference between Stilism and Anders22 reddening—only considering stars below 2.5 kpc—has systematic errors that increase with $E(B - V)_{A22}$ up to a maximum of ~ 1.6 mag for the highly extinct LOSs. Furthermore, M06 reddening estimates are only reliable up to a limited distance, as the column density increases and sources in the K band no longer have counterparts in the J band. The model presented by M06 then has limitations at large distances where the calculations depend on the parameters and assumptions of the authors. We, therefore, decide to take the safe path and use M06 reddening estimates only up to a distance of 3 kpc.

We found that G19 is consistent with Anders22 within the 68% confidence interval (approximately 1σ margin error of 0.12 mag), up to $E(B - V)_{A22} \sim 1.3$ mag (Figure 1, top left). The systematic difference scatters mostly below 0.3 mag for the entire IPS-GI sample, with very few stars scaling to a maximum of ~ 1 mag. Nevertheless, the systematic difference depends on the individual fields, e.g., we discuss in Section 6.4

⁵ <https://dustmaps.readthedocs.io/en/latest/#>

⁶ <https://stilism.obspm.fr/>

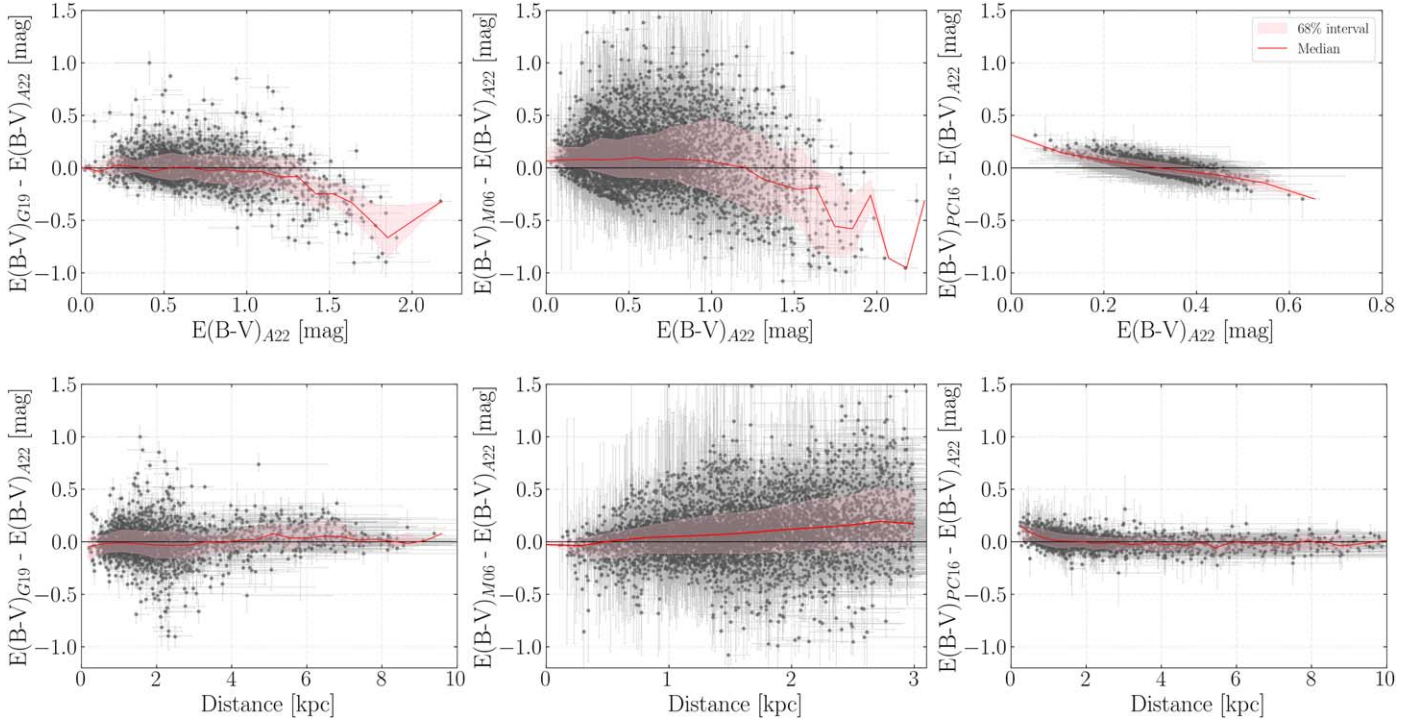


Figure 1. Systematic reddening difference of **G19** (left), **M06** (middle), and **PC16** (right) with **Anders22** shown as a function of **Anders22**'s reddening (top row) and distance (bottom row). Only the diffuse fields, i.e., *C2*, *C16*, *C36*, and *C37*, are used in the **PC16** comparison (right; see Table 1 and the explanation in Section 3.2). Red solid lines represent the median value of the difference, and the pink shaded area is the $\sim 1\sigma$ confidence interval delimited by the 16th and 84th percentiles.

the systematic reddening error of field *C2* observed between 0.14 and 0.16 mag depending on the dust map.

M06, on the other hand, is consistent with **Anders22** within a 1σ margin error of ~ 0.2 mag up to $E(B-V)_{A22} \sim 1.6$ mag (Figure 1, top middle). Moreover, **M06** reddening is often higher at $E(B-V)_{A22} \lesssim 1.2$ mag, the scatter scales up to 1 mag, and the uncertainties are extremely large. All of this results from the limitations of the method explained above.

The difference with **PC16** (top-right panel of Figure 1) shows a systematic error mostly below 0.2 mag throughout the entire range of reddening values. At $E(B-V)_{A22} < 0.3$ mag, **PC16** reddening is higher because it is integrated along longer pathlengths. At $E(B-V)_{A22} > 0.3$ mag, **PC16** reddening is often lower, which in addition to the increasing systematic error found above $E(B-V)_{A22} \sim 1.3$ mag in the **G19** and **M06** comparison, demonstrates that **Anders22** may be overestimating the reddening in the highly extinct LOSs.

The reddening difference as a function of distance in Figure 1 (bottom row) shows a median difference of **G19** (left), **M06** (middle), and **PC16** (right), with **Anders22** close to zero. The 1σ confidence interval of the difference is below ~ 0.1 mag, ~ 0.2 mag, and ~ 0.06 mag on average, respectively. **M06** reddening is systematically higher for longer LOSs and has significant errors. **PC16** reddening is up to ~ 0.16 mag higher at the most diffuse LOSs ($d < 1$ kpc), which may be due to the highest column density proven throughout the Galaxy. The scatter of **G19**'s difference around 2 kpc may be due to the systemic errors of the individual fields.

In summary, despite the different methods and bandwidths used, the limitations on distance, and sky coverage, the differences of **G19** and **PC16** with **Anders22** using all fields together are small ($E(B-V)_{A22} < 0.3$ mag). Although the difference scatters up to 0.2–0.3 mag (3σ of the reddening

difference) using the entire data set, it is important to mention that the systematic error observed in diffuse regions (e.g., *C2*, *C16*, and *C37*) is below 0.14 – 0.2 mag depending on the field and the dust map (see Section 6.4 for more details). Consequently, we must account for uncertainties of < 0.2 mag out to $E(B-V)_{A22} \sim 1.3$ mag depending on the field, and possibly a systematic error of maximum 1 mag only at high reddening, i.e., $E(B-V)_{A22} \gtrsim 1.3$ mag. Finally, from here on, we will refer to the **Anders22** reddening simply as $E(B-V)$.

3.3. Variations of the Extinction Curve

The extinction curve varies across the sky and along each sight line (Serkowski et al. 1975), as the total to selective extinction ratio map, R_V , presented by Schlafly et al. (2016), shows. Unfortunately, the R_V map, built with APOGEE spectroscopic data (Majewski et al. 2017), only covers the Northern sky. A reasonable assumption, however, is to take a constant value $R_V = 3.1$ (Savage & Mathis 1979; Fitzpatrick 2004), as we did to find the reddening using *V*-band extinction.

Nonetheless, going a step further, we can use the Schlafly et al. (2016) map to have a rough idea of how different values of R_V affect the polarization efficiency using the trends observed in the Northern sky. By doing so, we found that in the Northernmost fields, one can use $3.0 < R_V < 3.3$, whereas, in fields located at $360^\circ < l < 210^\circ$, the R_V values may be higher, $3.3 < R_V < 3.7$. Assuming an extreme R_V value for each case, we end up with higher polarization efficiencies in the Southernmost fields (i.e., an increase of $\sim 20\%$ of the value calculated with $R_V = 3.1$) and lower values in the Northernmost

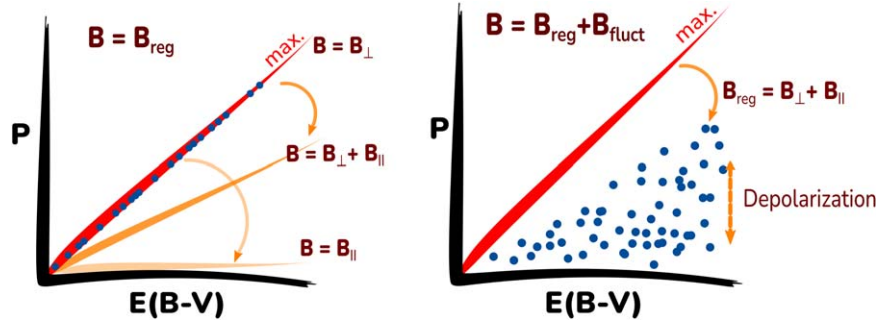


Figure 2. Polarization as a function of the reddening under different conditions of the ISM. Left: uniform magnetic field and constant/uniform dust properties. Right: magnetic field with uniform and fluctuating components, dust properties vary.

fields (i.e., a decrease of $\sim 5\%$ of the value calculated with $R_V = 3.1$).

4. The Relation between Reddening and Polarization

4.1. Basic Scenarios in the General ISM

Graphs of the linear polarization as a function of the reddening can be used to quantify the maximum starlight polarizing efficiency in the dusty ISM. In particular, the reddening increases monotonically with the interstellar dust column density, but this is not necessarily true for polarization. For instance, spherical and carbonaceous dust grains produce no polarization at all (Draine & Fraisse 2009), nor does dust in a magnetic field oriented along the line of sight. Moreover, small-scale and meso-scale structures, like turbulence or discrete objects, might change the magnetic field properties along the sight line. Consequently, the polarization produced by far interstellar dust clouds might be canceled out by foreground structures with different dust and magnetic field properties (i.e., depolarization) because the starlight polarization observed is a vector quantity averaged along the sight line. Therefore, the polarization efficiency depends on both the interstellar dust grains and the GMF properties.

Let us first consider the general diffuse ISM as an ideal scenario with uniform distribution and properties of elongated polarizing dust grains and a completely regular magnetic field, $\mathbf{B} = \mathbf{B}_{\text{reg}}$, that does not change along the sight line. Thus, one would expect a continuous linear increase in reddening and polarization with distance. Consequently, the relation between the degree of polarization and the reddening becomes a straight line, as in Figure 2 (red line in the left panel), with a steep slope for a GMF perpendicular to the sight line, $\mathbf{B}_{\text{reg}} = \mathbf{B}_{\perp}$, that decreases until the GMF become parallel to the sight line, as $\mathbf{B}_{\text{reg}} = \mathbf{B}_{\parallel}$.

As mentioned above, dust properties could vary, and the magnetic field can have different strengths, orientations, $\mathbf{B}_{\text{reg}} = \mathbf{B}_{\parallel} + \mathbf{B}_{\perp}$, and random fluctuations, $\mathbf{B} = \mathbf{B}_{\text{reg}} + \mathbf{B}_{\text{fluct}}$ (i.e., components with coherent scales smaller than the regular magnetic field scales), in reality. These variations can happen along the sight line and between LOSs themselves. All of this adds dispersion to the $P_V/E(B-V)$ relation. In other words, the variations in dust and magnetic field properties can cause smaller values of polarization relative to the optimum situation, or no polarization at all (see, e.g., models from Jones 1989; Jones et al. 1992). The polarization efficiency straight-line case ($\mathbf{B} = \mathbf{B}_{\text{reg}} = \mathbf{B}_{\perp}$) then becomes an upper limit or envelope, $[P_V/E(B-V)]_{\text{max}}$, that covers the measurements, as in Figure 2 (right).

We describe two general scenarios in Figure 2, but more complex ones may exist. For instance:

1. P and $E(B-V)$ may be constant along the sight line, which happens when we run out of dust grains at some distance. In this case, the polarimetry, dust grains, and GMF properties belong to some nearby polarizing dust structure that makes up all of our observed polarization and reddening.
2. Only P is constant in some regions along the sight line, whereas the reddening increases. So either there are no interstellar polarizing dust grains in some sections of the sight line, there is a significant parallel component of the GMF to the sight line, $\mathbf{B}_{\text{reg}} = \mathbf{B}_{\parallel}$, or there is a substantial fluctuating component of the large-scale GMF. All of these conditions can occur combined as well.

In essence, the degree of polarization as a function of the reddening in dense and turbulent ISM regions, e.g., molecular clouds, is different from the general diffuse ISM. Along highly extinguished LOSs, the dust and GMF properties vary considerably (see, e.g., Andersson et al. 2015), and polarization efficiency can constrain dust grain-alignment efficiency with the local magnetic field (see, e.g., Whittet et al. 2008; Jones & Whittet 2015; Draine & Hensley 2021). In contrast, the high polarization efficiency observed in different wavelengths in diffuse ISM regions (Andersson & Potter 2007; Pereyra & Magalhães 2007; Skalidis et al. 2018; Panopoulou et al. 2019; Planck Collaboration et al. 2020), and complex dust population models (Kim & Martin 1995) are all best explained with high alignment efficiency. In this case, if we can assume uniform/constant elongated dust grain properties and complete grain alignment in the general diffuse ISM, most variations in the polarization efficiency may be due to changes in the magnetic field intensity and geometry. For instance, a low polarization efficiency can be caused by GMF lines approximately parallel to the sight line, depolarization due to a fluctuating component of the GMF, or a combination of both. Meanwhile, high polarization efficiency would mean the presence of a significant regular GMF and a favorable alignment of the GMF with the plane-of-sky.

4.2. Calculating the Upper Envelope of the Polarization Efficiency

The upper limit of the polarization efficiency is calculated as the weighted 99th percentile, or the weighted 0.99 quantile (Section 4.2.3), of the $P_V/E(B-V)$ distribution (see, e.g., Figure 3) using only high-quality data (Section 2.5). This limit covers 99% of the weighted measurements, as shown, for example, in Figure 3, which is approximately a 3σ limit. The

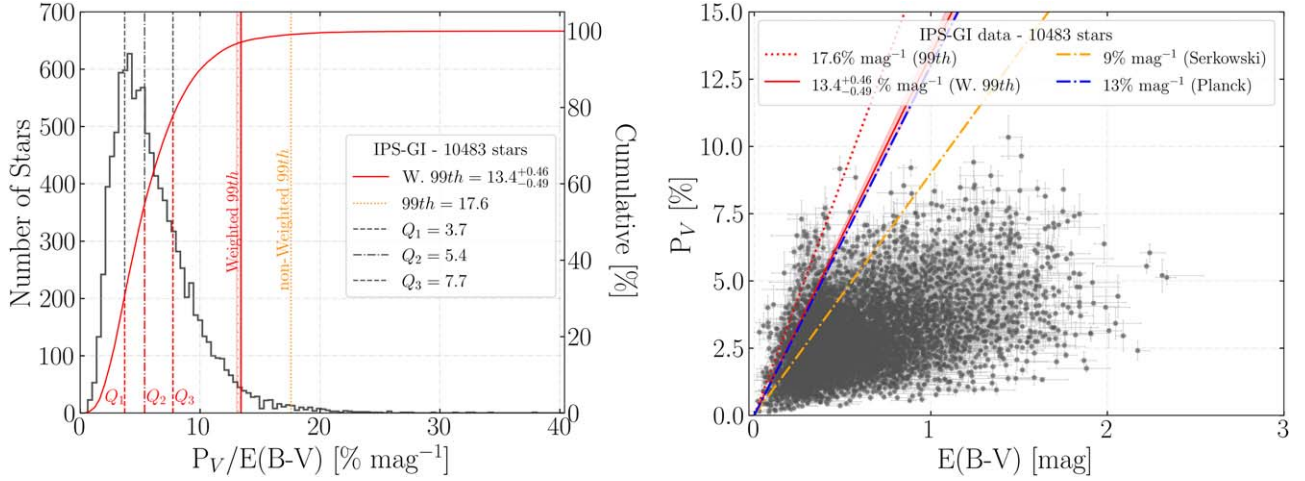


Figure 3. Left: polarization efficiency histogram of high-quality IPS-GI data. The cumulative percentage function is shown by the red curve. Dashed lines are the 0.25 (Q_1) and 0.75 (Q_3) quantiles, while the dotted-dashed line shows the 0.5 (Q_2) quantile or median value. Right: polarization degree as a function of the reddening. Upper limits of Serkowski and Planck are represented by the dotted-dashed lines in orange and blue, respectively. The red dotted line is the nonweighted 99th percentile, and the red solid line, with the underlying shaded region, is the weighted calculation with the 68% confidence interval.

nonweighted 99th percentile (the orange dotted line in the same figure) is often higher and very sensitive to outliers. A weighted calculation, on the other hand, can account for uncertainties in the measurements and performs better with outliers (see, e.g., robust estimation; Press et al. 1992). However, Bayesian methods often present their results with asymmetric errors. These errors arise from a nonlinear dependency of the results on a nuisance parameter (Barlow 2003), in our case, $E(B - V)$. Hence, any statistical calculation becomes nontrivial, and very few formulations exist for asymmetric errors (Barlow 2003; Erdim & Hudaverdi 2019). Furthermore, there is no straightforward method to estimate weighted statistics, such as quantiles or linear fits. Thus, more complicated techniques such as bootstrapping or Monte Carlo simulations are needed.

4.2.1. Error Propagation

In the propagation of asymmetric errors, the typical solution is to add in quadrature the two different errors separately, but there is no statistical justification for this. Barlow (2003) presented a method to add asymmetric uncertainties and accurately calculated some (few) statistics on the linear combinations of quantities. Still, the procedure may be not the same when the operation is different from an addition, e.g., a ratio. Unfortunately, Barlow (2003) did not have a solution for our specific problem. Lacking a more precise method, we calculate our errors through standard error propagation as

$$\sigma_{x/y}^{\pm} = \frac{x}{y} \sqrt{\left(\frac{\sigma_x^{\pm}}{x}\right)^2 + \left(\frac{\sigma_y^{\pm}}{y}\right)^2}. \quad (5)$$

4.2.2. Quantile Estimator

The quantiles divide the probability distribution function (PDF) of a particular range of measurements into p intervals with equal probability. The quantile function, also known as the percentile function or the inverse cumulative distribution function (CDF), allows finding the data value where the CDF crosses the k th quantile (with $k = 1, 2, \dots, p - 1$), i.e., the real

value that probability is the same as the k th quantile. Most statistical software packages⁷ use method 7 (or Type 7) defined by Hyndman & Fan (1996) as the quantile estimator. This quantile estimator can be expressed as (see, e.g., Hyndman & Fan 1996; Akinshin 2022, 2023):

$$Q(x, q_k) = \sum_{i=1}^n W_{n,i} \cdot x_i, \\ = x_{(\lfloor h \rfloor)} + (h - \lfloor h \rfloor)(x_{(\lfloor h \rfloor + 1)} - x_{(\lfloor h \rfloor)}), \quad (6)$$

where x_i is the i th measurement or order statistic,⁸ with $i = 1, 2, \dots, n$ for a total number of measurements n ; q_k is the k th quantile with values on $[0, 1]$; $W_{n,i}$ is the area of the k th interval of the PDF; and $\lfloor h \rfloor$ denotes the floor of the parameter h , which is the real value index to which the q_k quantile probability corresponds,

$$h = q_k(n - 1) + 1. \quad (7)$$

One can define a CDF function (F_7) such that,

$$F_7(u) = \begin{cases} 0, & \text{for } u < (h - 1)/n, \\ nu - h + 1, & \text{for } (h - 1)/n \leq u \leq h/n, \\ 1, & \text{for } h/n < u, \end{cases} \quad (8)$$

with the corresponding PDF $f_7(u) = F_7'(u)$, as the derivative of the CDF. Then,

$$W_{n,i} = F_7(r_i) - F_7(l_i). \quad (9)$$

In the nonweighted quantile estimation, we choose the edges of the k th interval to be

$$l_i = \frac{i - 1}{n} \quad \text{and} \quad r_i = \frac{i}{n}, \quad (10)$$

⁷ For instance R, NumPy, SciPy, among others.

⁸ The order statistics are, in simple words, the sorted measurements.

so all fragments have equal width $1/n$. Now, we define the m th moment as

$$Q_m(x, q_k) = \sum_{i=1}^n W_{n,i} \cdot x_i^m, \quad (11)$$

where $m = 1, 2, \dots$ denotes the moments, and the first moment is the quantile (see Akinshin 2023, for more details). The uncertainty of the quantile can be obtained from the first and second moments. So, the standard error of the calculation is⁹

$$\sigma_{Q(x, q_k)} = \sqrt{Q_2(x, q_k) - Q_1^2(x, q_k)}. \quad (12)$$

4.2.3. Weighted Quantile Estimator

The weighted T7 quantile can be considered the generalization of the nonweighted estimator (Equations (9), (10), and (11), which would be the particular case when all of the weights are equal to 1 (Akinshin 2023). First, the total sum of the weights defined as $S_n(w) = \sum_{i=1}^n w_i > 0$, for $i = 1, 2, \dots, n$, is always positive and different from zero (assuming $w_i \geq 0$). Second, the partial sum of weights $S_i(w)$ is defined as the cumulative sum of the order statistics until the i th measurement. Hence, the interval of width proportional to the weights, i.e., equal to $w_i/S_n(w)$, should be between

$$l_i^* = \frac{S_{i-1}(w)}{S_n(w)}, \quad r_i^* = \frac{S_i(w)}{S_n(w)}, \quad (13)$$

where $S_0(w) = 0$ is assumed. When all weights are equal (i.e., $w = 1$), then, $l_i = l_i^*$ and $r_i = r_i^*$. Furthermore, we consider n^* as the weighted or effective sample size (Wiegand 1968):

$$n^* = \frac{\left(\sum_{i=1}^n w_i\right)^2}{\sum_{i=1}^n w_i^2}, \quad (14)$$

which redefines the h^* parameter from Equation (7) and the CDF $F_7^*(u)$ in Equation (8). Then, we evaluate the weighted interval edges in the latter equation to calculate the area of the weighted interval, $W_{n,i}^*$, as in Equation (9). Finally, we obtain the weighted quantile estimation $Q^*(x, q_k)$ with Equation (11) ($m = 1$). The standard error of the weighted quantile can be computed with the weighted first and second moments, as in Equation (12) (see Akinshin 2023, for more details).

4.2.4. Weighted Quantile with Asymmetric Errors

The weighted quantile estimation presented in Section 4.2.3 assumes symmetric uncertainties, but this is not our case. $P_V/E(B - V)$ has asymmetric errors as in Equation (5); therefore, we used the bootstrap technique to calculate the weighted 0.99 quantile, or 99th percentile.

The bootstrap method uses the original sample to recalculate the weighted statistic in several iterations (e.g., we use $N = 10,000$) with different weights each time. This should not be confused with re-sampling, as we are not using a subsample of the original data. We are rather recalculating our statistic N times with a measurement error re-sampled from a two-sided exponential probability density function (PDF)

defined for each data point:

$$\frac{1}{2\lambda_{1,2}} \exp\left\{\frac{-|x - \mu|}{\lambda_{1,2}}\right\}, \quad (15)$$

with $\mu = 0$ and $\lambda_{1,2} = \sigma_{\pm}/\sqrt{2}$, where σ_{\pm} are the asymmetric uncertainties and the discontinuity at zero is avoided when re-sampling. We used the inverse of the measured errors, $1/\sigma$ (Press et al. 1992), as weights for the quantile estimation (Section 4.2.3), where σ is the re-sampled error. In our specific case, a two-sided exponential PDF and the respective inverse of the error weight proved to be more robust against outliers than an asymmetric Gaussian PDF and the inverse of the squared error weight, i.e., $w = 1/\sigma^2$ (see, e.g., the comparison between Gaussian and exponential probability errors in Press et al. 1992). The latter approach turned out to be a heavy weight on the highest signal-to-noise measurements that yielded underestimated upper envelopes.

Finally, the outcome of the iterations is a distribution from which we can obtain some metrics, such as the median value and its 68% confidence interval. These metrics are computed for the entire IPS-GI sample or any subsample (i.e., individual fields) to determine our results on the polarization efficiency upper limit. The confidence interval is useful to identify potential outliers in polarization efficiency, i.e., high $P_V/E(B - V)$ values that can affect our statistics and increase the uncertainty of the calculations, especially in small distributions. The variability of potential outliers is assessed in Section 2.6, and Appendices A.1 and A.2.

5. Results

We present our results on the polarization efficiency for the entire IPS-GI sample and individual fields using Anders22 reddening. Additionally, we show results on the relation between the polarization efficiency and Galactic coordinates.

5.1. $P_V/E(B - V)$ Upper Envelope of All IPS-GI Data

Initially, the polarization efficiency upper envelope and its confidence interval were calculated including all IPS-GI objects having good-quality data. Figure 3 (right) shows the degree of polarization as a function of the reddening for all IPS-GI data. The upper envelope of the polarization efficiency, i.e., the weighted 99th percentile, is $13.4_{-0.49}^{+0.46} \% \text{ mag}^{-1}$. This result is in good agreement with the maximum value from Planck Collaboration et al. (2020), $13\% \text{ mag}^{-1}$, and far above the value from Serkowski et al. (1975), $9\% \text{ mag}^{-1}$, (both studies using all-sky samples). Nonetheless, the weighted 99th percentile found with the entire IPS-GI sample (Figure 3) should not be considered an average for the highest polarization efficiency since, toward each field (i.e., each sight line), the GMF and the interstellar dust have different properties. The upper limit of the polarization efficiency should, therefore, vary across the Galaxy. We must then study the IPS-GI fields individually as follows.

5.2. $P_V/E(B - V)$ Upper Envelope per IPS-GI Field

We present the weighted polarization efficiency upper limits calculated for each of the 34 IPS-GI fields in Figure 4. The results are also shown in Table 1 and Figure 5 (the complete figure set is available). A total of 20 IPS-GI fields have

⁹ Here we used the property of the variance of a variable X : $\text{Var}(X) = E[X^2] - E[X]^2$.

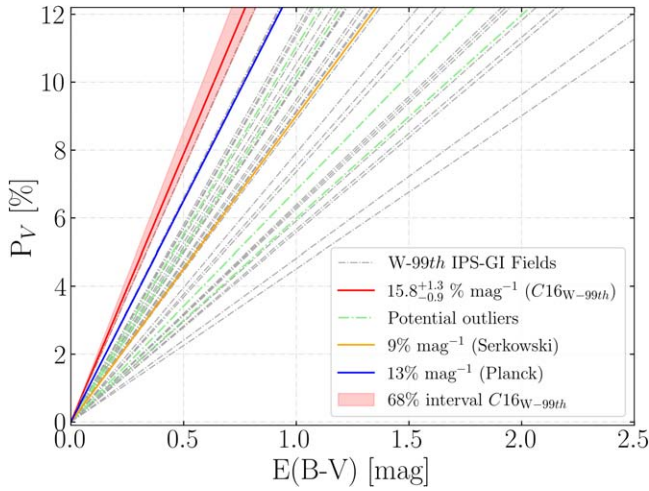


Figure 4. Weighted $P_V/E(B-V)$ upper limit per IPS-GI field (gray dotted-dashed lines). The red solid line and pink area are the weighted polarization efficiency upper limit and confidence interval in field *C16*. The light-green dotted-dashed lines are slopes affected by potential outliers in polarization efficiency (see the figure set for more details). The blue and orange solid lines are, respectively, Planck’s and Serkowski’s limits.

polarization efficiencies similar to, or above, the $9\% \text{ mag}^{-1}$ limit. Five of them are higher than the Planck Collaboration et al. (2020) maximum upper limit of $13\% \text{ mag}^{-1}$: two slopes are within the red-shaded area, near the highest value, in Figure 4, and other two are very close to the blue slope in the same figure; see Table 1 for more details.

We mitigated the impact of potential outliers in our results by using weighted quantile estimations (as described in Section 4.2). In small samples, however, we still see some steep slopes with significant uncertainties (the light-green dotted-dashed lines in Figure 4, and Table 1) that may be affected by poor statistics (e.g., see the plots of *C30*, *C42*, *C43*, and *C56* in the figure set for more details). In Section 6.4 we discuss how the same fields present similar issues in the calculations of the upper limits with *G19* and *M06* reddening.

5.3. Maximum Upper Limit of $P_V/E(B-V)$

Figure 5 shows the degree of polarization as a function of the reddening of fields *C2*, *C16*, and *C37*. These fields have the highest upper limits of polarization efficiency in our sample, around $\sim 15\% \text{ mag}^{-1}$ (see Table 1 and Figure 4). Their distributions cluster in a very narrow range of low reddening, between $0.1 \text{ mag} \lesssim E(B-V) \lesssim 0.5 \text{ mag}$. Meanwhile, the degree of polarization expands in a long range between $\sim 0.5\%$ and $\sim 7\%$. The maximum weighted polarization efficiencies are estimated using more than 500 high-quality measurements in each of these fields (see Table 1). This makes our results very robust, even against potential outliers in polarization efficiency (corresponding to $\sim 2\%$ of the stars on each field). Hence, we adopt the weighted $P_V/E(B-V)$ upper limit observed in field *C16*, $[P_V/E(B-V)]_{C16} = 15.8^{+1.3}_{-0.9} \% \text{ mag}^{-1}$, as the maximum polarization efficiency in our sample.

5.4. $P_V/E(B-V)$ Upper Envelope as a Function of Galactic Coordinates

Significant variations in polarization efficiency are observed with Galactic latitude and longitude (Figure 6). IPS-GI fields at intermediate latitudes ($|b| > 7.5$) and within Galactic longitudes

$270^\circ\text{--}360^\circ$ have the highest polarization efficiency observed (see top panel of Figure 6). On the other hand, low polarization efficiencies are found toward Galactic longitudes $\sim 15^\circ\text{--}45^\circ$, and perhaps $l \sim 220^\circ\text{--}275^\circ$. Fields with a low number of stars and potential outliers in polarization efficiency (Section 4.2), such as *C30*, *C42*, *C43*, and *C56*, likely have overestimated $P_V/E(B-V)$ upper limits with significant uncertainties, as visible in the bottom row of Figure 6 (see also Table 1). Thus, their polarization efficiency may be significantly lower and consistent with nearby fields. Versteeg et al. (2023) showed that in the corresponding Galactic longitudes, the degree of polarization of IPS-GI data is also high and low, respectively (see, e.g., their Figure 11). In fact, Fosalba et al. (2002) observed similar trends in their average optical polarization with LOSs across the entire sky.

6. Discussion

6.1. Variations of $P_V/E(B-V)$ across the Galaxy

C2, *C16*, and *C37* are the closest IPS-GI fields to the ideal scenario outlined in Figure 2 (left). The LOSs pointing toward $|b| > 7.5$ largely avoid the most extinct regions of the Galactic thin disk, as the extinction map of Vergely et al. (2022) shows (Figure 7, top). In a face-on view of the same map (Figure 7, bottom), the LOSs—especially field *C16*—seem to be almost perpendicular to the large Galactic structures. Assuming that the magnetic field lies along those structures, it should be largely perpendicular to these LOSs as well. However, the constant reddening and polarization intensity observed from a certain distance (e.g., see scatter plots in Figure 8), as well as the lack of significant structures in the *V*-band extinction density profiles within the same range of distances (e.g., top panel of the same figure), prove that the LOSs leave the Galactic thin disk at some point (see vertical orange dotted-dashed lines), and the polarizing dust structure is expected to be within the first ~ 1 kpc. Hence, the presence of a nearby regular magnetic field in the plane-of-sky and the lack of—or very little—additional dust after 1 kpc might explain the high alignment of the polarization vectors within the field of view and the remarkably small dispersion of the polarization angle (Figure 9). Furthermore, the highly polarized stars observed above 1 kpc in *C2* may be explained by small variations in density within the nearby dust screen (see, e.g., Figures 5 and 8). However, we have no evidence of such small structures so far. The properties described above and the high polarization efficiency (Figure 4 and Table 1) prove that fields *C2*, *C16*, and *C37* are ideal to define the maximum $P_V/E(B-V)$.

In the Galactic neighborhood ($d < 1$ kpc), intermediate-latitude stars have on average a higher degree of polarization ($P_V \sim 2.7\%$) than the stars in low-latitude fields ($P_V \sim 1.8\%$). Nevertheless, the reddening is almost the same in all directions for all nearby stars due to the low column density built up in short LOSs, e.g., 99% of IPS-GI stars within $d < 1$ kpc have $E(B-V) \leq 0.8$ mag. In consequence, the polarization efficiency is higher in intermediate-latitude fields (e.g., *C2*, *C16*, and *C37*) than in low-latitude fields (see the top and bottom-right panels of Figure 6). The above result could indicate either the presence of an increasingly regular magnetic field on the plane-of-sky, less depolarization, a change in polarizing dust properties, or any combination of these conditions toward higher latitudes. However, none of these possible explanations can be proven yet, and the number of intermediate-latitude fields in our sample is too

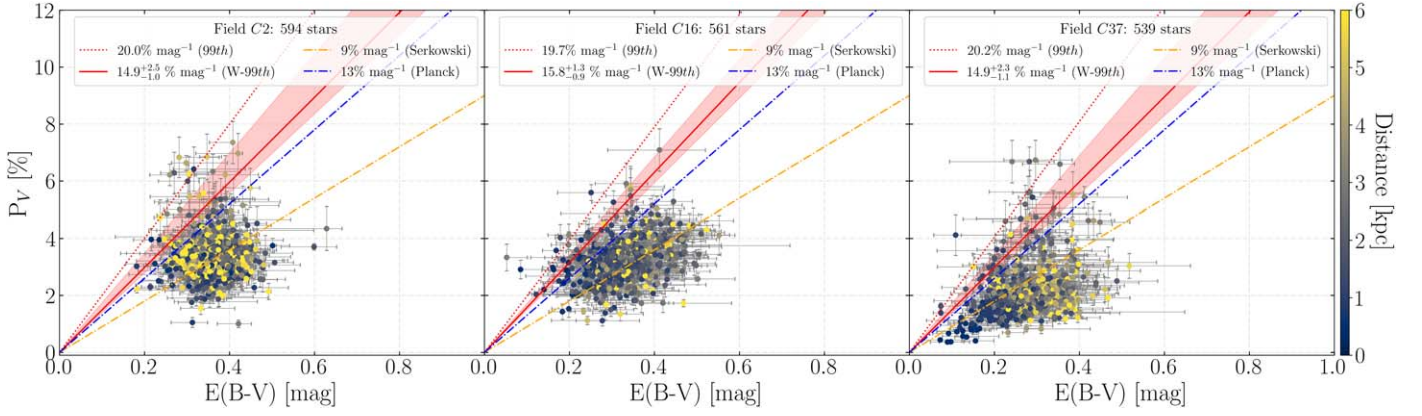


Figure 5. Degree of polarization as a function of reddening in fields *C2* (left), *C16* (middle), and *C37* (right). Stars are colored by distance with the color range truncated at 6 kpc for better visualization. The solid red lines and the pink areas are the weighted $P_V/E(B - V)$ upper limits with their respective 68% confidence interval. The dotted red lines are the nonweighted upper limits. The blue and orange dotted–dashed lines show Planck’s and Serkowski’s upper limits, respectively. (The complete figure set (31 images) is available.)

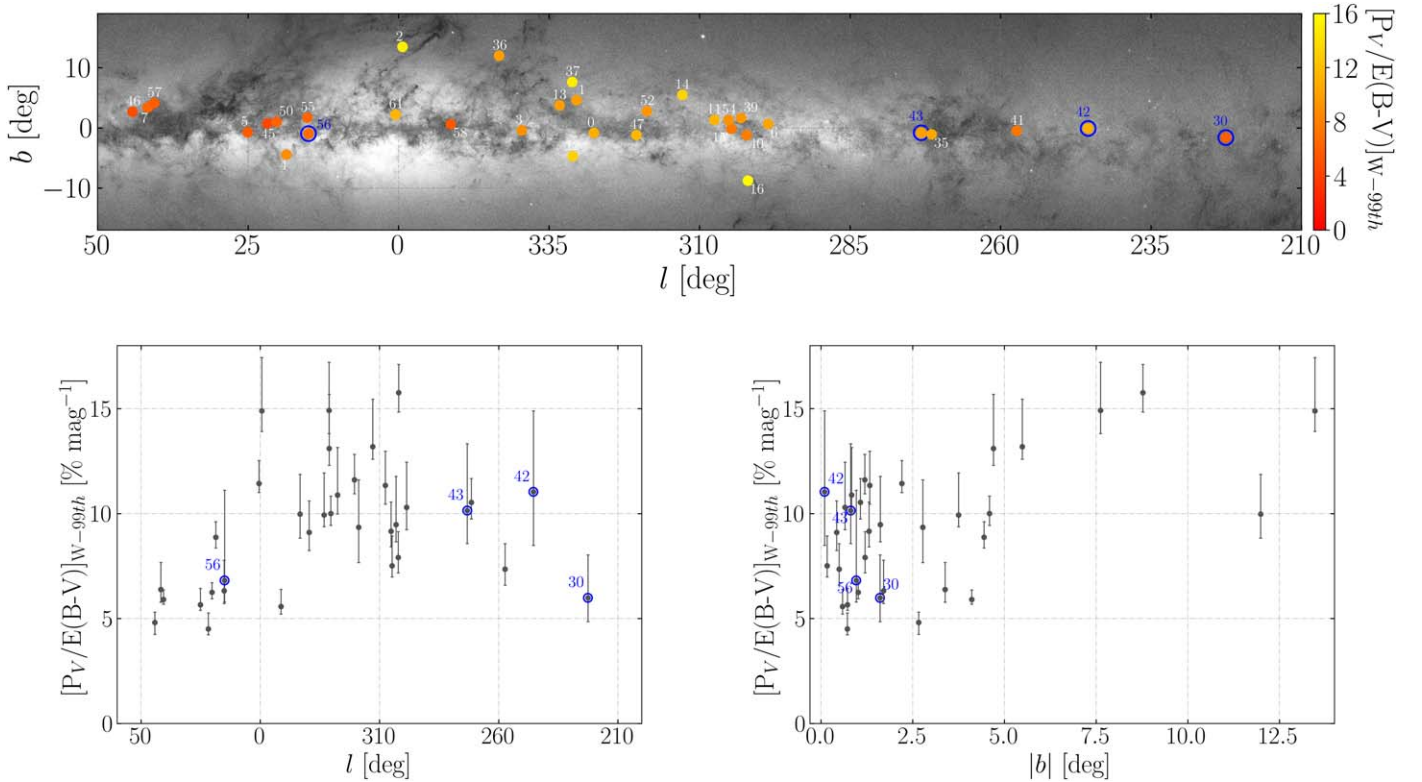


Figure 6. Top: sky plot showing the IPS-GI fields location colored by the weighted $P_V/E(B - V)$ upper limits. The turquoise circles are unreliable upper limits due to potential outliers. The background image is the optical emission of the Galaxy adapted from ESA/Gaia/DPAC. Bottom: weighted $P_V/E(B - V)$ upper limits with Galactic longitude (left), and absolute Galactic latitude (right). Error bars show the 68% confidence interval of the weighted 99th percentile (Section 4.2).

low to reach a conclusion. More optical polarization observations at intermediate-latitude regions are needed.

At $d > 1$ kpc, intermediate-latitude LOSs leave the Galactic thin disk (see the vertical orange dotted–dashed line in Figure 8) and encounter little or no polarizing dust at all (see top panels of Figure 6); then, the starlight polarization of distant stars is produced only in the nearby (foreground) dust structures. Contrarily, low-latitude LOSs run into more interstellar dust. For instance, 99% of these stars have $E(B - V) \leq 1.6$ mag on average. The starlight polarization may increase but so does the

reddening (and perhaps the depolarization); therefore, the polarization efficiency is lower than in intermediate-latitude fields.

6.2. $P_V/E(B - V)$ Models with Galactic Longitude

To get an idea of the expected variability of $P_V/E(B - V)$ with Galactic longitude, we introduce a simple toy model. We assume that the dust density is constant and dust properties are uniform. We model the large-scale magnetic field in the solar

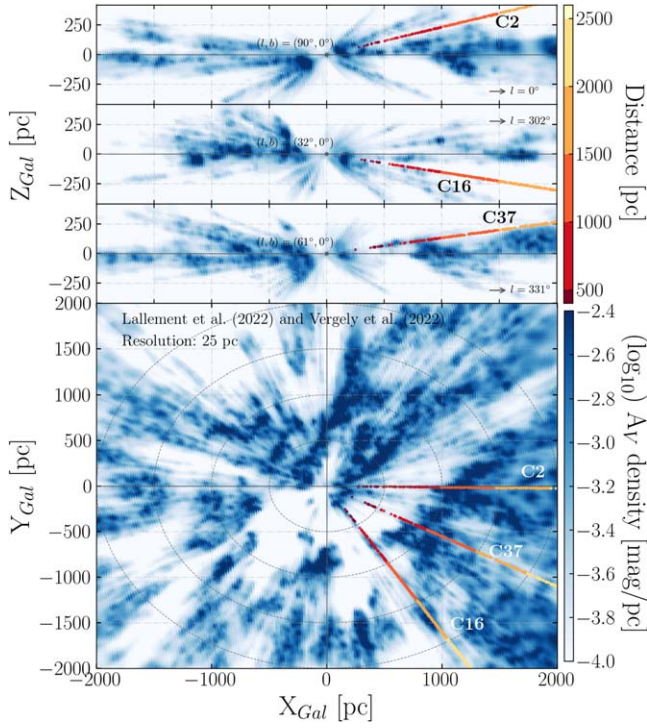


Figure 7. Intermediate Galactic latitude LOSs (C2, C16, and C37) on top of the Lallement et al. (2022) and Vergely et al. (2022) dust map, at 25 pc resolution, of the nearby Galaxy ($d < 2$ kpc). The blue color bar is the V -band extinction density in log space. The red color bar is the distance of the stars in parsecs. Top: edge-on views of the Galaxy centered at different (l, b) coordinates depending on the sight line. Bottom: face-on view of the Galaxy centered at the Sun at $(0, 0)$ pc. The Galactic center, $(l, b) = (0, 0)$, is at $(8200, 0)$ pc, toward the right, in all maps.

neighborhood as a uniform field of constant orientation, directed along the local pitch angle at the Sun. For nearby stars, the modeled magnetic field direction corresponds well to a spiral magnetic field, whereas, for distant stars, the assumption holds less well.

Then, the only aspect that determines the dependence of polarization efficiency on Galactic longitude is the variation of polarizability as a function of the inclination i of the magnetic field with the line of sight. We use two different dust models to determine the dependence on i : Jones et al. (1992) and Rodrigues et al. (1997). Both models incorporate dust partially aligned with the magnetic field.

First, Jones et al. (1992) defined the effective polarization power as $\eta = \kappa_{\perp} / \kappa_{\parallel}$, where κ_{\perp} (κ_{\parallel}) is the extinction coefficient perpendicular (parallel) to the long axis of the grain. The polarization efficiency is proportional to the differential polarization per unit pathlength dx as

$$dP = \frac{1 - \eta}{1 + \eta} \kappa dx = \frac{1 - \eta}{1 + \eta} d\tau, \quad (16)$$

and η depends on the inclination angle i as

$$\eta(i) = \frac{\eta_p + (1 - \eta_p) \cos(i) + R}{1 + R}, \quad (17)$$

where η_p is the polarizing power of aligned grains, and R is the ratio of the extinction of the unaligned component to that of the aligned component, $\kappa_u / \kappa_{a\parallel}$. The polarization efficiency can

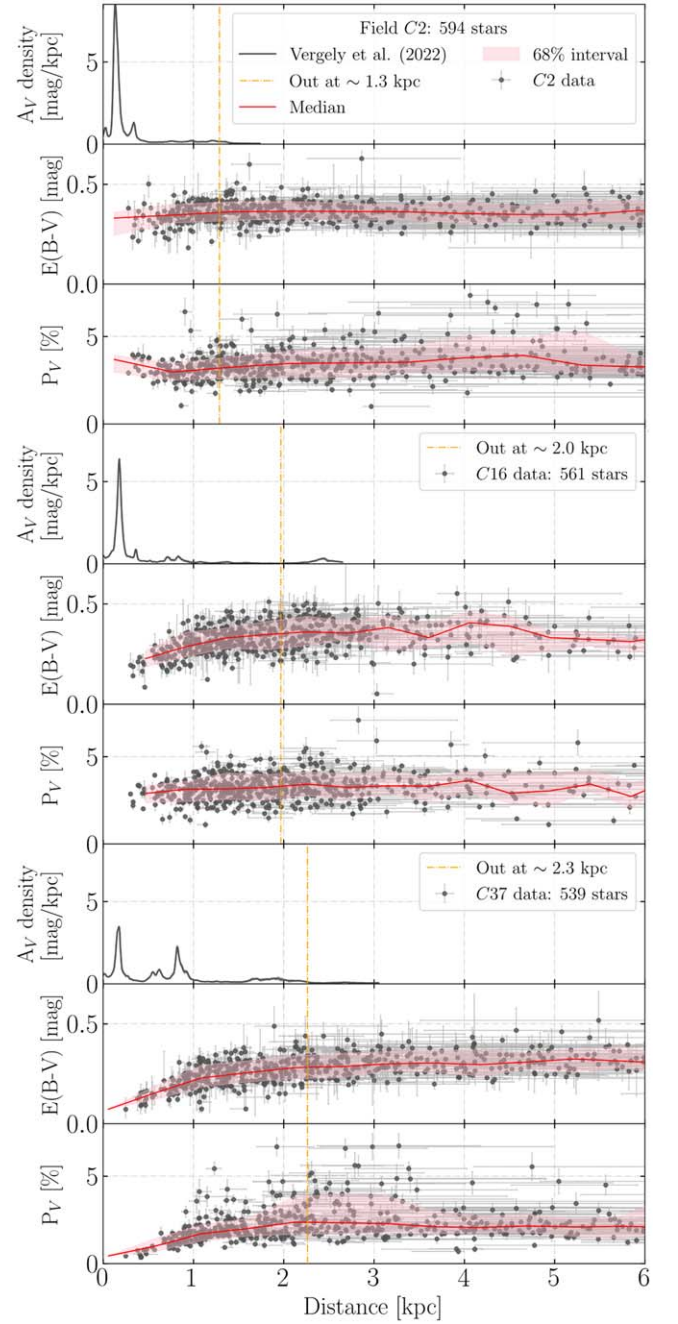


Figure 8. Differential optical extinction profile (25 pc resolution) from Vergely et al. (2022) and Lallement et al. (2022; top row), reddening (middle row), and polarization intensity (bottom row), as a function of distance in fields C2 (left), C16 (middle), and C37 (right). The red solid line is the median value. The pink shaded area is the 16th–84th confidence interval. The vertical orange dotted–dashed line is the approximated distance at which the sight line leaves the Galactic thin disk, assuming a scale height of 300 pc.

then be defined as

$$\frac{P}{E(B - V)} = \frac{3.1}{1.086} \frac{P}{\tau} \approx \frac{3.1}{1.086} \frac{1 - \eta(i)}{1 + \eta(i)}, \quad (18)$$

assuming a total to selective extinction ratio $R_V = 3.1$. Jones et al. (1992) constrained the parameters η_p and R by assuming maximum polarization for an inclination angle $i = 90^\circ$. They concluded that although η_p and R are degenerate, η depends

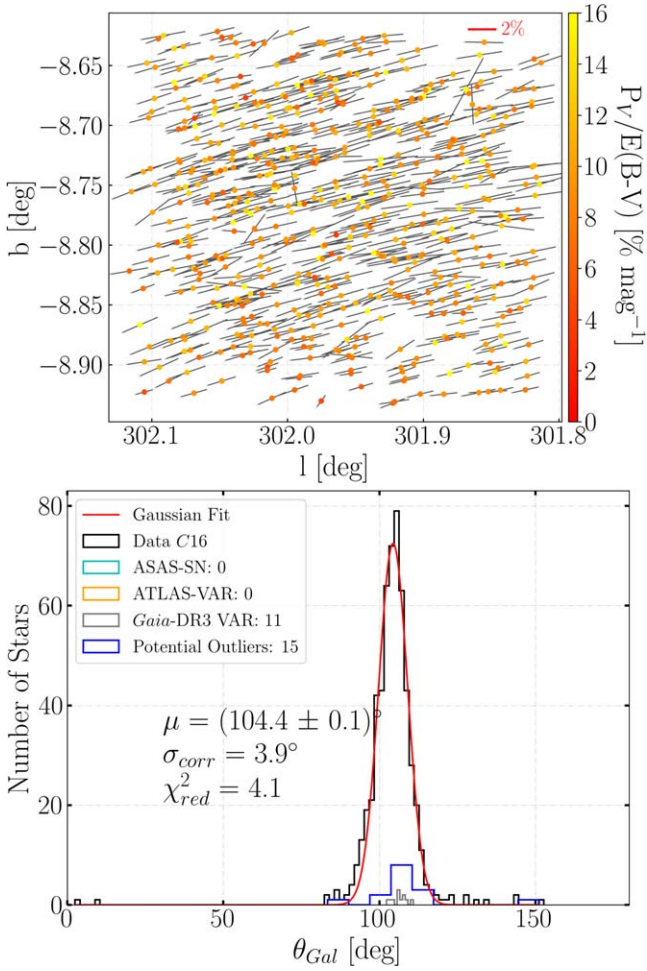


Figure 9. Top: polarization vectors in field *C16* colored by the polarization efficiency. Bottom: polarization angle (in the Galactic frame) of the same field. The dispersion is corrected in quadrature by the measured error average as in Pereyra & Magalhães (2007).

very little on their exact values for the allowed parameter ranges. They used $(\eta_p, R) = (0.5, 3)$, which we will adopt here as well.

Second, Rodrigues et al. (1997) developed a dust model of spherical and cylindrical grains for the Milky Way and Small Magellanic Cloud data: infrared to ultraviolet extinction and optical polarization in broad bands. The dichroic absorption of the Galactic model was derived for different inclination angles by Santos-Lima et al. (2023, in preparation), who found a best-fit relation of

$$\frac{P}{E(B-V)} \propto 1 - \sin^{1.57}(i). \quad (19)$$

This model has an arbitrary scaling, which we took to match the scaling in the previous model.

In our simple picture, the inclination angle is related to Galactic longitude as $i = \pi/2 - l + p$, where p is the pitch angle, which we vary between -10° and -25° (Vallée 2015). Figure 10 presents the final models of polarization efficiency with Galactic longitude. The toy models indeed reproduce the high values at $330^\circ \leq l \leq 360^\circ$, and low $P_V/E(B-V)$ at $l \sim 30^\circ - 80^\circ$ and possibly $l \sim 235^\circ - 285^\circ$, where the LOSs are expected to be parallel to the magnetic field. High-pitch

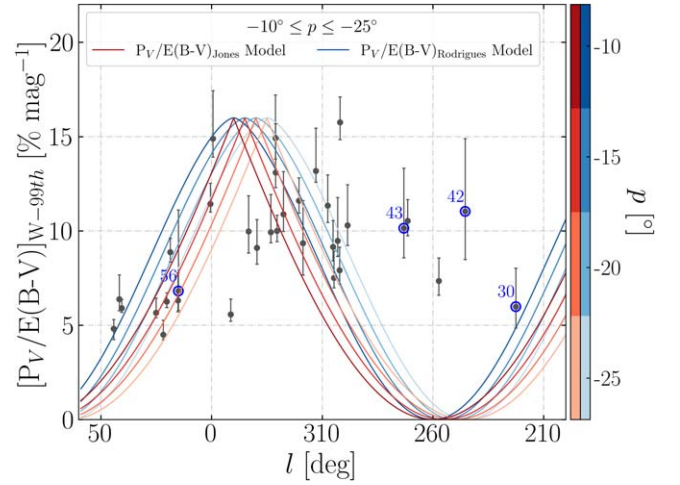


Figure 10. Polarization efficiency upper limits with Galactic longitude. The red and blue curves are the toy models for different pitch angles, p .

angles appear to best reproduce our observations of high polarization efficiency, also agreeing with the local pitch angle of the large-scale dust structures observed in the Vergely et al. (2022) maps (Figure 7). Nevertheless, the models fail to describe our observations around $l \sim 285^\circ$. These are the cases of fields *C35*, *C41*, *C42*, and *C43*, in which the polarization efficiencies are not the lowest. In addition to being potential outliers, it is clear proof that the magnetic field is not parallel to the LOS in these particular fields. Toward these Galactic longitudes, we find the Gum nebula, in which radio polarimetry properties were studied in detail by Purcell et al. (2015), who showed that the entire structure has a polarization angle between 43° and 55° at an adopted distance of ~ 450 pc. Although the magnetic field orientation in field *C41* agrees with the values found by Purcell et al. (2015), there is no evidence of dust inside the nebula. In fact, the polarizing dust structures are likely behind it (see, e.g., the lower panel of Figure 7 in the south-southwest direction).

Despite all simplifications and assumptions made, the toy models are close to IPS-GI observations. This remains true even when considering other widely used dust models (see, e.g., Andersson et al. 2015, and references therein), such as the approximation of the observed polarization to $\propto \cos^2(\gamma)$ from Lee & Draine (1985) dust grain models, which gives a slightly broader curve. Nevertheless, our data show that $P_V/E(B-V)$ is also a function of the latitude as well as of the longitude. Additionally, nearby ($d < 1$ kpc) small-scale and meso-scale structures are critical in GMF modeling. A future version of these models must consider the different inclinations of the magnetic field along the sight line and variations with Galactic latitude.

6.3. Implications for Dust Models

A comprehensive interstellar dust model should be able to reproduce the observed extinction, emission, and polarization in the entire spectral domain. It should therefore account for dust grains composition, size distributions, and alignment properties (Rodrigues et al. 1997; Jones et al. 2015; Hensley & Draine 2021, and references therein). For instance, Hensley & Draine (2021) synthesized the most important observational

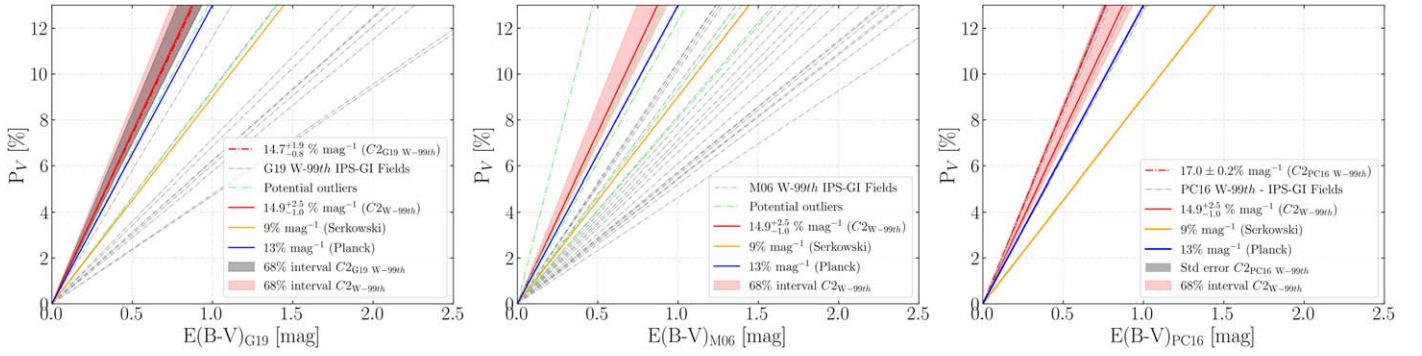


Figure 11. Similar to Figure 4 but using **G19** (left), **M06** (middle), and **PC16** (right) reddening to calculate the upper limits on each IPS-GI field (gray dashed lines). The red dashed lines show the upper limit of field **C2**. Light-green dashed lines are unreliable upper envelopes due to potential outliers or unreliable reddening measurements. For **PC16**, only the intermediate-latitude fields are plotted; see Section 3.2.

constraints for multiwavelength dust models on the diffuse ISM, showing the importance of polarization efficiency due to the origin of optical polarization (short axis of elongated interstellar dust grains aligned preferably parallel to the local magnetic field). Rodrigues et al. (1997) studied the interstellar ultraviolet extinction and optical polarization of the Small Magellanic Cloud using dust models based on the Mathis et al. (1977) prescription, with different grain size distributions and composition. They also fitted the “standard” Galactic extinction and polarization curves. The latter was built assuming a maximum polarization efficiency of $9\% \text{ mag}^{-1}$. The best fit for the wavelength dependencies of polarization and extinction determines the grain size ranges, alignment properties, composition distribution, and the depletion of Si and C in the ISM. Interestingly, the resulting maximum polarization efficiency of these models is greater than $9\% \text{ mag}^{-1}$. Rodrigues et al. (1997) presented models for three specific angles (10° , 30° , and 60°) between the magnetic field and the plane-of-sky. Extrapolating their results for an angle of 0° , using Equation (19), we obtained polarizing efficiencies between $14.4\% \text{ mag}^{-1}$ and $16.5\% \text{ mag}^{-1}$ (depending on the model), in close agreement with our results for the maximum polarization efficiency of $15.8\% \text{ mag}^{-1}$. However, a more careful prediction for the grain properties that could produce such high polarizing efficiency requires new modeling.

6.4. Dependency of $P_V/E(B-V)$ on Dust Maps

Previous studies have shown that the polarization efficiency upper limit may be highly dependent on the dust map used (see, e.g., Panopoulou et al. 2019). It is noteworthy that the weighted polarization efficiency upper envelopes calculated (for the sake of comparison) with the reddening of **G19**, $[P_V/E(B-V)]_{G19_{W-99th}}$, and **PC16**, $[P_V/E(B-V)]_{PC16_{W-99th}}$ (Figure 11), also show values higher than $13\% \text{ mag}^{-1}$, and very consistent with the upper limits observed in fields **C2**, **C16**, and **C37** using **Anders22** reddening. Nonetheless, one should be aware that low-resolution dust maps may lead to polarization efficiency overestimation since multiple polarization measurements can have the same pixel value, and the information on the small-dense structures is lost.

On the other hand, the weighted upper limits calculated with **M06** reddening, $[P_V/E(B-V)]_{M06_{W-99th}}$ (Figure 11, middle panel), are lower in average. Few exceptions must be carefully compared (light-green slopes in Figure 11: fields **C42** and **C56** in the left, and **C14**, **C43**, **C55**, **C56**, and **C61** in the middle) since poor statistics, and sometimes poor

measurements (see, e.g., the discussion about the dust maps quality in Section 3.2), still affect the weighted $P_V/E(B-V)$ upper-limit calculation, leading to large uncertainties (Section 4.2). Unfortunately, we are missing information on fields that are not covered by the aforementioned databases, not to mention the limitations of dust maps explained in Section 3.2.

In particular, **G19** and **PC16** have maximum weighted upper limits in field **C2** ($14.7^{+1.9}_{-0.8}\% \text{ mag}^{-1}$ and $17.0\% \pm 0.2\% \text{ mag}^{-1}$, respectively) remarkably consistent (within the confidence interval) with the maximum value $15.8^{+1.3}_{-0.9}\% \text{ mag}^{-1}$ (Section 5.3). In the range of $0.2 \text{ mag} \leq E(B-V) \leq 0.5 \text{ mag}$ of field **C2**, systematic errors of $\sim 0.16 \text{ mag}$ and $\sim 0.14 \text{ mag}$ are expected with respect to **G19** and **PC16**, respectively (see, e.g., Figure 12). Meanwhile, at closer distances ($d < 2 \text{ kpc}$), **Anders22**’s reddening is $\sim 0.05 \text{ mag}$ higher than **G19**’s. Given that the highest polarization efficiency is measured within the first kiloparsec, the systematic error in reddening between **G19** and **Anders22** would contribute toward lower values of **Anders22** reddening and, therefore, toward higher polarization efficiency.

Figure 13 shows the difference between the weighted polarization efficiency upper limits calculated with the different dust maps considered in this work (Section 3.1). The difference between the **M06** and **Anders22** weighted upper limits have a large scatter, often below $\sim 5\% \text{ mag}^{-1}$, which may reflect the limitations of **M06** dust map. The difference between $[P_V/E(B-V)]_{G19_{W-99th}}$ and $[P_V/E(B-V)]_{W-99th}$, on the other hand, is lower and very close to zero with very small scatter. In Sections 3.2 and 5.2, and Figure 13, we showed that **Anders22** and **G19** are the most consistent, which is somewhat expected since the **G19** dust map was used in the construction of **Anders22**’s extinction prior. Even in fields with large uncertainties, both calculations are equally affected by the potential outliers, i.e., **C30**, **C42**, and **C56**, except **C43** where **G19** does not have measurements. Due to the small difference, it is very likely that the trend would be the same in fields where there is no data from **G19** yet. In fact, high polarization efficiency calculated with an updated version of the **G19** dust map would be expected in the intermediate Galactic latitude regions, where $[P_V/E(B-V)]_{W-99th}$ is high as well.

The intermediate-latitude fields, where multiple dust maps are available, show high polarization efficiency regardless of the dust map used, i.e., **G19** and **PC16**. Recall that **PC16** is only comparable with **Anders22** at intermediate and high latitudes, i.e., in diffuse LOSs, as explained in Section 3.2. The values

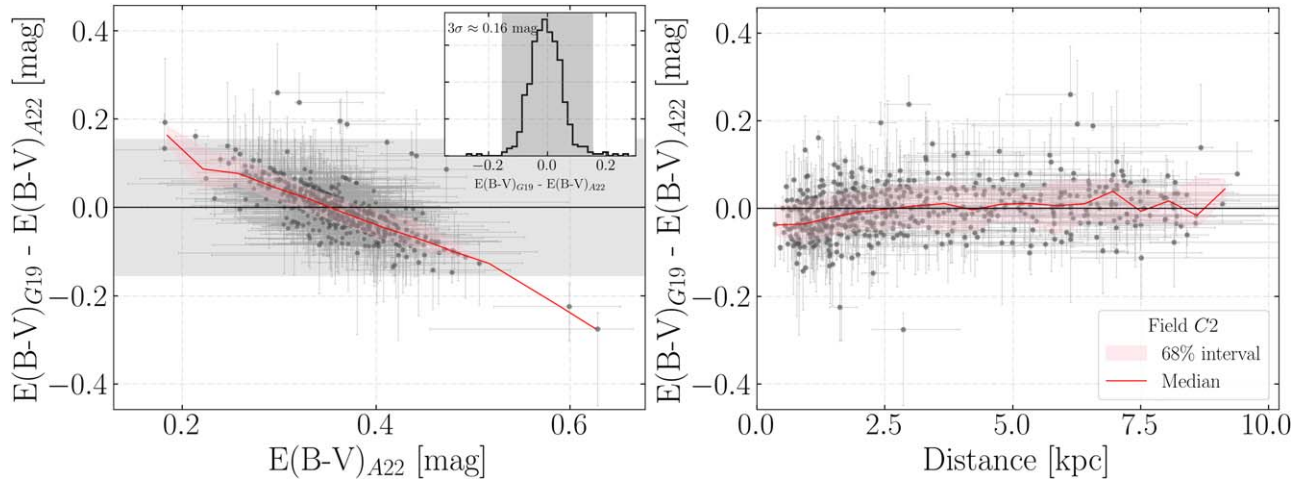


Figure 12. Similar to the systematic reddening differences of Figure 1 but only for field C2. The histogram shows the distribution of the difference and the values under the 3σ limit (the gray-shaded area).

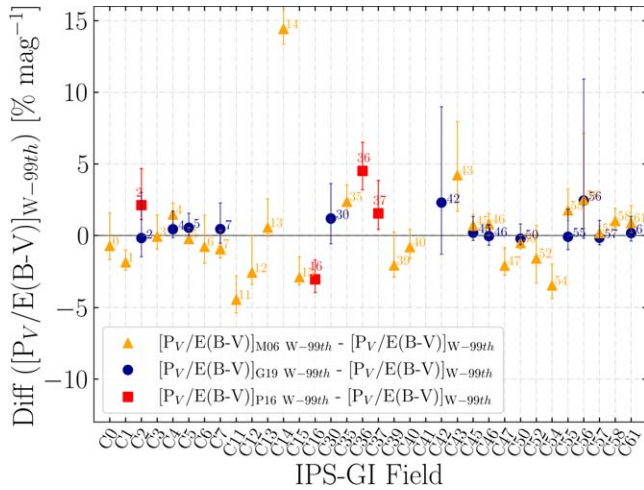


Figure 13. Systematic difference between the weighted polarization efficiency upper envelopes calculated with G19 (dark-blue circles), M06 (orange triangles), and PC16 (red squares) reddening, and those calculated with Anders22 reddening.

found in this work for the $[P_V/E(B-V)]$ upper limits, which are higher than past estimations, are unlikely to be atypical measurements and are very consistent with the factors compared here.

6.5. Correlation with the Polarization Angle Dispersion

The polarization angle in most of the IPS-GI fields is remarkably coherent (see, e.g., Figure 9); i.e., approximately 84% of the fields showed a dispersion of the polarization angle below 15° , and 50% is below 10° (Versteeg et al. 2023). The dispersion in polarization angle indicates the fluctuations in the orientation of the plane-of-sky component of the magnetic field. For nearby stars ($d < 1$ kpc), the projected size of the IPS-GI fields is smaller than 5 pc. Both scales are consistent with interstellar turbulence and fluctuations due to small-scale structures (e.g., supernova remnants, H II regions, and cold dark clouds). However, for distant objects ($d > 1$ kpc), and considering the small size of the IPS-GI fields in relation to the long pathlengths, these variations in magnetic field orientation

are expected to be dominated by meso-scale fluctuations along the LOS.

Figure 14 shows that fields with high polarization efficiency often have a lower dispersion in polarization angle than low polarization efficiency fields. The anticorrelation between the polarization angle dispersion and the weighted polarization efficiency upper envelope is marginal (the Spearman correlation coefficient is -0.60 , above 3σ , and the two-tailed p -value is 2.0×10^{-4}). However, the anticorrelation with the weighted median of $P_V/E(B-V)$ is more significant (the correlation coefficient is -0.74 and the two-tailed p -value is 5.2×10^{-7}).

This result strengthens the idea of a highly regular magnetic field in the plane-of-sky, low depolarization, and a small random magnetic field component in IPS-GI fields with high polarization efficiencies. It is also consistent with the anticorrelation found by Planck Collaboration et al. (2020) between the polarization angle dispersion and the polarization fraction, which they attribute to depolarization by the turbulent magnetic fields of different structures along the sight line. Nevertheless, Y. Doi et al. (2023, submitted) demonstrated that such depolarization may be also due to multiple, local regular magnetic field structures with very different orientations (90° offset).

7. Summary

We used optical polarization maps of 34 sky fields sampling the general ISM. Each field covers an area of 0.3×0.3 square and has polarization measurements of typically hundreds of stars. These measurements were combined with the optical extinction and Gaia-EDR3 distances from Anders22 to study the polarization efficiency in the ISM.

We propose a new method to estimate the polarization efficiency upper limit considering the asymmetric uncertainties of the measurements. This method is robust against outliers and avoids misleading estimations of $[P_V/E(B-V)]_{\max}$. The upper limit carries information on dust and interstellar magnetic field properties. It is a powerful diagnostic when comparing regions in the sky and an important parameter for interpreting starlight polarization measurements to numerical simulations of the magnetized ISM (e.g., see Santos-Lima et al. 2023, in preparation). Moreover, $[P_V/E(B-V)]_{\max}$ represents an

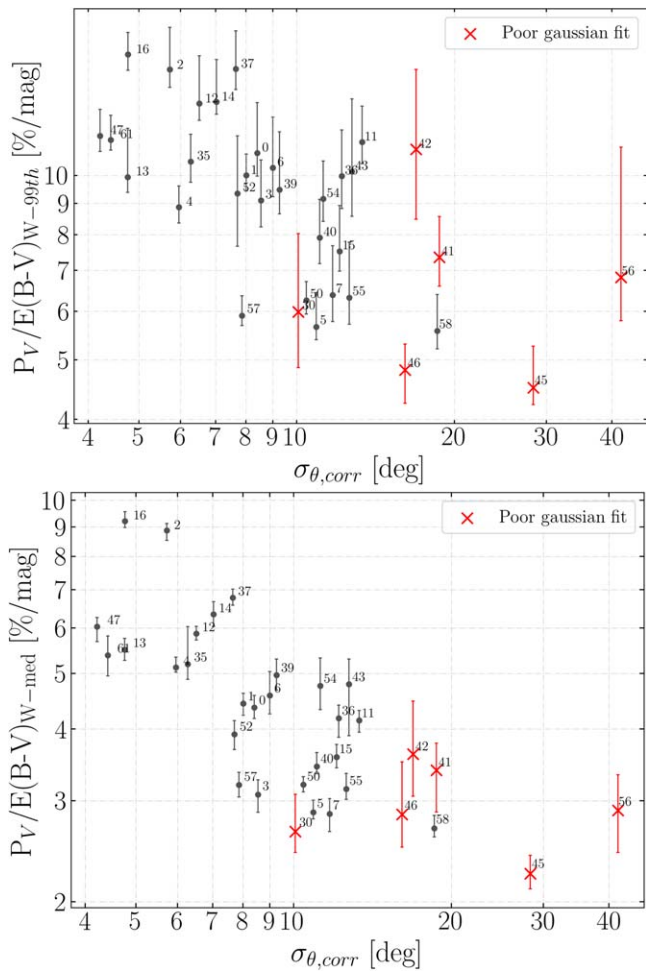


Figure 14. Weighted polarization efficiency upper envelope (top) and weighted median polarization efficiency (bottom) as a function of the dispersion of the polarization angle corrected by the average of the measured errors as in Pereyra & Magalhães (2007). Bad Gaussian fits of the polarization angle distribution are indicated with red “X” markers.

important observational constraint for interstellar dust models (Section 6.3).

The maximum polarization efficiency in our sample is $[P_V/E(B-V)]_{C16} = 15.8^{+1.3}_{-0.9} \text{ mag}^{-1}$. This high polarization efficiency, observed in a number of intermediate-latitude fields ($b > 7.5$), is higher than Planck’s upper limit ($13\% \text{ mag}^{-1}$), which is averaged over the whole high-latitude sky, independently of the dust map used (Anders22; G19; M06; PC16). The high $P_V/E(B-V)$ upper envelope is consistent with a nearby ($d < 1 \text{ kpc}$) highly regular GMF on the plane-of-sky and the lack of depolarization due to additional dust structures beyond 1 kpc, as was demonstrated by the observed degree of polarization and reddening with distance, and the anticorrelation with the polarization angle dispersion.

The IPS-GI data show variable polarization efficiencies in the general ISM with Galactic coordinates broadly consistent with toy models, in Galactic longitude, that assume a uniform local magnetic field with a reasonable pitch angle consistent with the literature. However, our observations demonstrate that interstellar optical polarization is highly dependent on nearby small-scale and meso-scale structures. Moreover, the toy models do not account for $P_V/E(B-V)$ variations with Galactic latitude. Therefore, comprehensive modeling is

needed to accurately explain variations of the polarization efficiency across the Galaxy.

The authors thank the careful reading by the anonymous referee, whose review helped improve this paper.

Y.A.A. acknowledges Dr. M. Riello for his contributions in discussions about the photometric validation of Gaia-EDR3 and the determination of the *variability proxy*, a key Gaia metric to find potential variable sources.

Y.A.A. is also grateful to Dr. Andrey Akinshin for his insights and the mathematical development of a weighted quantile estimator.

The authors acknowledge the Interstellar Institute’s program “With Two Eyes” and the Paris-Saclay University’s Institut Pascal for hosting discussions that nourished the development of the ideas behind this work.

Over the years, IPS data have been gathered by a number of dedicated observers, to whom the authors are very grateful: Flaviane C. F. Benedito, Alex Carciofi, Cassia Fernandez, Tibério Ferrari, Livia S. C. A. Ferreira, Viviana S. Gabriel, Aiara Lobo-Gomes, Luciana de Matos, Rocio Melgarejo, Antonio Pereyra, Nadili Ribeiro, Marcelo Rubinho, Daiane B. Seriacopi, Fernando Silva, Rodolfo Valentim, and Aline Vidotto.

Y.A.A., M.H., and M.J.F.V. acknowledge funding from the European Research Council (ERC) under the European Union’s Horizon 2020 research and innovation program (grant agreement No. 772663).

C.V.R. acknowledges support from *Conselho Nacional de Desenvolvimento Científico e Tecnológico - CNPq* (Brazil) (Proc. 310930/2021-9).

A.M.M.’s work and optical/NIR polarimetry at IAG have been supported over the years by several grants from São Paulo state funding agency FAPESP, especially 01/12589-1 and 10/19694-4. A.M.M. has also been partially supported by the Brazilian agency CNPq (grant 310506/2015-8). A.M.M.’s graduate students have been provided with grants over the years from the Brazilian agency CAPES.

Finally, this work has made use of data from the European Space Agency (ESA) mission Gaia (<https://www.cosmos.esa.int/gaia>), processed by the Gaia Data Processing and Analysis Consortium (DPAC, <https://www.cosmos.esa.int/web/gaia/dpac/consortium>). Funding for the DPAC has been provided by national institutions, in particular, the institutions participating in the Gaia Multilateral Agreement.

Facility: LNA:BC0.6m.

Software: Astropy (Astropy Collaboration et al. 2013, 2018), Matplotlib (Hunter 2007), NumPy (Harris et al. 2020), SciPy (Virtanen et al. 2020).

Appendix Variable Sources

In the following sections, we identify variable sources in the IPS-GI catalog and run diagnostics to evaluate their impact in our results.

A.1. Known Variable Sources in IPS-GI Catalog

Variable stars may have a polarization component that is intrinsic or produced by circumstellar phenomena other than the dichroic extinction of interstellar dust. In essence, variable stars may be an issue for our polarimetry analysis in the general ISM since they can add unreliable measurements

(see Section 2.6). Hence, we cross-matched the IPS-GI catalog with three different variable stars catalogs to identify these sources in our data set. The catalogs considered are: the ATLAS-VAR (Heinze et al. 2018) using a $2''$ margin, the ASAS-SN (Jayasinghe et al. 2018, 2019a, 2019b, 2020; Christy et al. 2023) with $2''$ and $G = 2$ mag margins, and the Gaia-DR3 (Eyer et al. 2022) variable stars using the Gaia-DR3 `source_id` parameter. We found 79 matches with ASAS-SN, 37 with ATLAS-VAR (only dubious probability below 0.6; see Section 4.2 in Heinze et al. 2018), and 807 with the Gaia-DR3 variable stars catalog (only “real” variables; see `vari_classifier_result` parameter explanation in Eyer et al. 2022). A total of 294 variable stars passed all quality filters described in Section 2.5, 19 of which are in more than one of the above databases (see Table A1). The variables reported by Versteeg et al. (2023) within the IPS-GI catalog did not pass our quality filters (Section 2.5). The final 294 variable sources do not seem to affect our results. Only 21 of them coincide with some potential outliers in polarization efficiency (see Section 4.2.4), and few (three) have deviations in polarization angle and polarization fraction above 3σ from the median distribution on each IPS-GI field (Figure A1, left).

A.2. The Gaia-EDR3 Variability Proxy

Riello et al. (2021) introduced a new Gaia-EDR3 metric called the *variability proxy*, which essentially corresponds to the estimated fractional error of a specific band on a single astrometric field (see their definition in their Appendix F). This metric performs very well to identify, for instance, extended sources such as galaxies (see, e.g., Figure F.2. of Riello et al. 2021), and it could be useful for identifying potential variable sources as well. We calculated the *variability proxy* in the G

band using **Gaia-EDR3** parameters as follows:

$$A_{\text{proxy } G} = \sqrt{\text{phot_g_n_obs}} \times \frac{\text{phot_g_mean_flux_error}}{\text{phot_g_mean_flux}}, \quad (\text{A1})$$

where `phot_g_n_obs` is the number of Gaia observations in the G band, `phot_g_mean_flux` is the mean G -band flux, and `phot_g_mean_flux_error` is the corresponding mean flux error. We compare in Figure A1 (right) the *variability proxy* as a function of the G -magnitude with the expected mean magnitude error in the G band (see, e.g., top panel of Figure 14; Riello et al. 2021), for a single Gaia observation. Additionally, we included the variable stars identified in the cross-matched lists with ASAS-SN, ATLAS, and Gaia-DR3 databases (see Section A.1).

The fractional errors in magnitude of the IPS-GI stars regularly follow the expected mean error for the G band, except for some deviations that scale from 0.5 mag for the brightest sources to 1.5 mag for the faintest sources. High fractional errors due to low flux measurements and noisy-crowded backgrounds are expected in faint stars. The variable stars have high fractional errors and are far from the mean magnitude error model, proving that the *variability proxy* is good to confirm variable sources or identify candidates. Furthermore, the potential outliers in polarization efficiency (see Section 4.2.4) are mostly faint stars consistent with the expected mean Gaia magnitude error. These sources do not have fractional errors deviating above 0.5 mag except for one particular source (black triangle at $G \approx 8$), which turns out to be one of the few potential outliers confirmed to be a variable star (Figure A1, right). In conclusion, we cannot clearly identify variable stars as IPS-GI outliers in the degree of polarization per reddening unit, nor say what exactly causes these outliers.

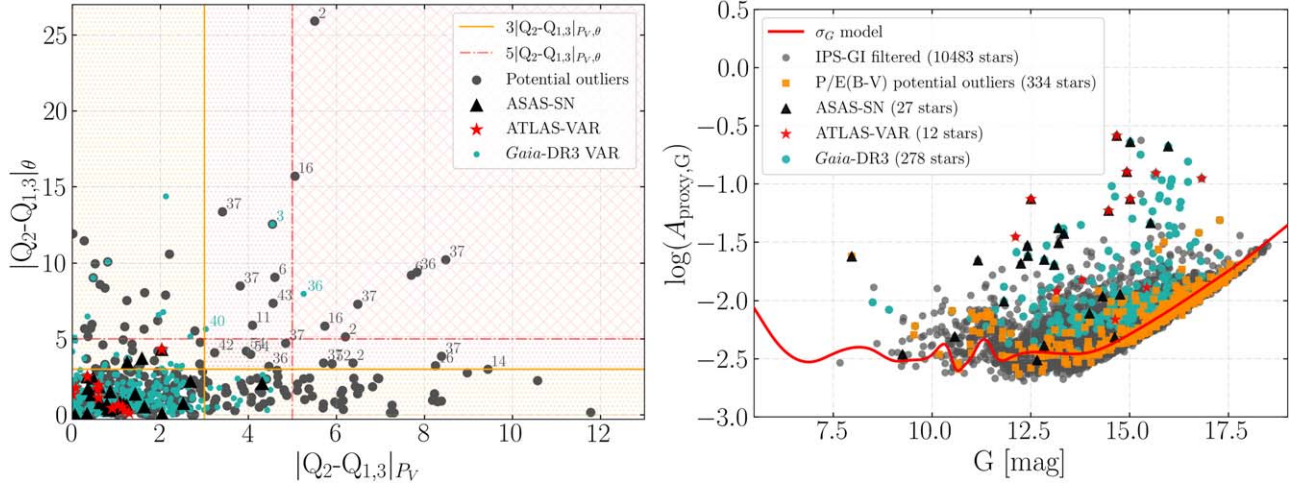


Figure A1. Left: deviations from the median value in polarization fraction and polarization angle of potential outliers in polarization efficiency (Section 4.2) and variable stars known in the IPS-GI database (Appendix A.1). The deviations from P and θ are the modulus of the difference between the median and the first or the third quantile in the distributions. Right: the logarithm of the *variability proxy* as a function of the G -band magnitude of IPS-GI data (blue dots). The red solid line is the logarithm of the expected mean G -magnitude error. The orange squares are potential outliers in polarization efficiency (Section 4.2.4). The black triangles and red stars are variable sources identified in the filtered cross-matched lists with ASAS-SN and ATLAS-VAR databases (Section A.1).

Table A1
Variable Stars in IPS-GI Catalog

Gaia-EDR3 ID	R.A. J2000 (deg)	Decl. J2000 (deg)	IPS-GI Field	Class	References
(1)	(2)	(3)	(4)	(5)	(6)
5884688765646295808	238.93509	-54.55096	0	(EA) Detached Algol-type binaries	(1), (3)
5986010102181385472	236.85535	-48.541686	1	Eclipsing binary	(3)
4126224902887846912	253.74885	-21.981876	2	(ROT) Rotational modulation	(1), (3)
4126267100963020928	253.72496	-21.763218	2	(RRAB) Fundamental mode RR Lyrae	(1), (2), (3)
4126253799432188544	253.74466	-21.792309	2	Compact companion	(3)
4103505354883822464	280.27874	-14.817128	4	(EW) W Ursae Majoris-type binaries	(1), (2), (3)
4103502258157032960	280.36007	-14.84001	4	(DBH) Distant binary, half period	(2), (3)
4252660532440869248	279.78211	-7.357264	5	(CBH) Close binary, half period	(2), (3)
5868675615759940224	202.50417	-61.089469	11	(YSO) Young stellar objects	(1)
5868656649182615040	202.71103	-61.337477	11	(GCAS) γ Cassiopeiae variables	(1)
5868651662671280768	202.51935	-61.348392	11	(EB) β Lyrae-type binaries	(1), (3)
5928955550488284416	247.94232	-54.966693	12	Eclipsing binary	(3)
5872309948348868480	210.90681	-56.057494	14	Rotation modulation	(3)
6022987502845965568	243.16885	-34.587574	36	(RRAB) Fundamental mode RR Lyrae	(1), (3)
6055566650847818368	192.89953	-61.246276	39	(ROT) Rotational modulation	(1), (3)
5313359983854184448	140.63481	-51.170444	43	(L) Irregular variables	(1)
5876965589814204160	228.79787	-58.944918	47	Main-sequence (MS) oscillators	(3)
5893111467061840640	222.32234	-56.301996	52	(EB) β Lyrae-type binaries	(1), (3)
4097791983182736128	275.45374	-16.457443	56	(EW) W Ursae Majoris-type binaries	(1), (2), (3)
4311099919049980416	282.79372	8.816396	57	(EW) W Ursae Majoris-type binaries	(1), (2), (3)

Note. Example list of cross-matched variable sources that passed our quality filters (Section 2.5). The complete table is available upon request to the author. Columns: (1) Gaia-EDR3 source id, (2) R.A. J2000 coordinate, (3) Decl. J2000 coordinate, (4) IPS-GI field id, (5) Database classification (of the first reference in column (6), and (6) Source database reference. The full table is available in machine-readable format. A portion is shown here for guidance regarding its form and content.

References. (1) ASAS-SN, Jayasinghe et al. (2018, 2019a, 2019b, 2020), (2) ATLAS-VAR, Heinze et al. (2018), (3) Gaia-DR3 variable stars, Eyer et al. (2022) and references therein).

(This table is available in its entirety in machine-readable form.)

ORCID iDs

Y. Angarita  <https://orcid.org/0000-0001-5016-5645>
M. J. F. Versteeg  <https://orcid.org/0000-0003-0400-8846>
M. Haverkorn  <https://orcid.org/0000-0002-5288-312X>
C. V. Rodrigues  <https://orcid.org/0000-0002-9459-043X>
A. M. Magalhães  <https://orcid.org/0000-0002-1580-0583>
R. Santos-Lima  <https://orcid.org/0000-0001-6880-4468>
Koji S. Kawabata  <https://orcid.org/0000-0001-6099-9539>

References

- Akinshin, A. 2022, arXiv:2208.13459
Akinshin, A. 2023, arXiv:2304.07265
Anders, F., Khalatyan, A., Queiroz, A. B. A., et al. 2022, *A&A*, 658, A91
Andersson, B. G., Lazarian, A., & Vaillancourt, J. E. 2015, *ARA&A*, 53, 501
Andersson, B. G., & Potter, S. B. 2007, *ApJ*, 665, 369
Astropy Collaboration, Price-Whelan, A. M., Sipőcz, B. M., et al. 2018, *AJ*, 156, 123
Astropy Collaboration, Robitaille, T. P., Tollerud, E. J., et al. 2013, *A&A*, 558, A33
Barlow, R. 2003, arXiv:physics/0306138
Beck, R., & Wielebinski, R. 2013, in *Planets, Stars and Stellar Systems. Volume 5: Galactic Structure and Stellar Populations*, ed. T. D. Oswalt & G. Gilmore, Vol. 5 (Dordrecht: Springer), 641
Beresnyak, A., & Lazarian, A. 2019, *Turbulence in Magnetohydrodynamics* (Berlin: De Gruyter)
Capitanio, L., Lallement, R., Vergely, J. L., Elyajouri, M., & Monreal-Ibero, A. 2017, *A&A*, 606, A65
Christy, C. T., Jayasinghe, T., Stanek, K. Z., et al. 2023, *MNRAS*, 519, 5271
Clarke, D., & Stewart, B. G. 1986, *VA*, 29, 27
Draine, B. T., & Friaese, A. A. 2009, *ApJ*, 696, 1
Draine, B. T., & Hensley, B. S. 2021, *ApJ*, 919, 651
Erdim, M. K., & Hudaverdi, M. 2019, in *AIP Conf. Ser.* 2178, Turkish Physical Society 35th International Physics Congress (TPS35) (Melville, NY: AIP) 030023
Eyer, L., Audard, M., Holl, B., et al. 2022, arXiv:2206.06416
Fitzpatrick, E. L. 2004, in *ASP Conf. Ser.* 309, *Astrophysics of Dust*, ed. A. N. Witt, G. C. Clayton, & B. T. Draine (San Francisco, CA: ASP), 33
Fosalba, P., Lazarian, A., Prunet, S., & Tauber, J. A. 2002, *ApJ*, 564, 762
Gaia Collaboration, Brown, A. G. A., Vallenari, A., et al. 2018, *A&A*, 616, A1
Gaia Collaboration, Brown, A. G. A., Vallenari, A., et al. 2021, *A&A*, 649, A1
Green, G. 2018, *JOSS*, 3, 695
Green, G. M., Schlafly, E., Zucker, C., Speagle, J. S., & Finkbeiner, D. 2019, *ApJ*, 887, 93
Harris, C. R., Millman, K. J., van der Walt, S. J., et al. 2020, *Natur*, 585, 357
Heiles, C. 2000, *AJ*, 119, 923
Heinze, A. N., Tonry, J. L., Denneau, L., et al. 2018, *AJ*, 156, 241
Hensley, B. S., & Draine, B. T. 2021, *ApJ*, 906, 73
Hunter, J. D. 2007, *CSE*, 9, 90
Hyndman, R. J., & Fan, Y. 1996, *AmSci*, 50, 361
Jayasinghe, T., Kochanek, C. S., Stanek, K. Z., et al. 2018, *MNRAS*, 477, 3145
Jayasinghe, T., Stanek, K. Z., Kochanek, C. S., et al. 2019a, *MNRAS*, 486, 1907
Jayasinghe, T., Stanek, K. Z., Kochanek, C. S., et al. 2019b, *MNRAS*, 485, 961
Jayasinghe, T., Stanek, K. Z., Kochanek, C. S., et al. 2020, *MNRAS*, 491, 13
Jones, T. J. 1989, *ApJ*, 346, 728
Jones, T. J., Bagley, M., Krejny, M., Andersson, B. G., & Bastien, P. 2015, *AJ*, 149, 31
Jones, T. J., Klebe, D., & Dickey, J. M. 1992, *ApJ*, 389, 602
Jones, T. J., & Whittet, D. C. B. 2015, in *Interstellar Polarization*, ed. L. Kolokolova, J. Hough, & A.-C. Levasseur-Regourd (Cambridge: Cambridge Univ. Press), 147, doi:10.1017/CBO9781107358249.009
Kim, S.-H., & Martin, P. G. 1995, *ApJ*, 444, 293
Lallement, R., Babusiaux, C., Vergely, J. L., et al. 2019, *A&A*, 625, A135
Lallement, R., Capitanio, L., Ruiz-Dern, L., et al. 2018, *A&A*, 616, A132
Lallement, R., Vergely, J. L., Babusiaux, C., & Cox, N. L. J. 2022, *A&A*, 661, A147

- Lee, H. M., & Draine, B. T. 1985, *ApJ*, **290**, 211
- Magalhães, A. M., Benedetti, E., & Roland, E. H. 1984, *PASP*, **96**, 383
- Magalhães, A. M., de Oliveira, C. M., Carciofi, A., et al. 2012, in AIP Conf. Ser. 1429, *Stellar Polarimetry: from Birth to Death*, ed. J. L. Hoffman, J. Bjorkman, & B. Whitney (Melville, NY: AIP), 244
- Magalhães, A. M., Pereyra, A., Melgarejo, R., et al. 2005, in ASP Conf. Ser. 343, *Astronomical Polarimetry: Current Status and Future Directions*, ed. A. Adamson et al. (San Francisco, CA: ASP), 305
- Magalhães, A. M., Rodrigues, C. V., Margoniner, V. E., Pereyra, A., & Heathcote, S. 1996, in ASP Conf. Ser. 97, *Polarimetry of the Interstellar Medium*, ed. W. G. Roberge & D. C. B. Whittet (San Francisco, CA: ASP), 118
- Majewski, S. R., Schiavon, R. P., Frinchaboy, P. M., et al. 2017, *AJ*, **154**, 94
- Marshall, D. J., Robin, A. C., Reylé, C., Schultheis, M., & Picaud, S. 2006, *A&A*, **453**, 635
- Mathis, J. S., Rumpl, W., & Nordsieck, K. H. 1977, *ApJ*, **217**, 425
- Naghizadeh-Khouei, J., & Clarke, D. 1993, *A&A*, **274**, 968
- Panopoulou, G. V., Hensley, B. S., Skolidis, R., Blinov, D., & Tassis, K. 2019, *A&A*, **624**, L8
- Pereyra, A., & Magalhães, A. M. 2007, *ApJ*, **662**, 1014
- Planck Collaboration Int. X. X. I., Ade, P. A. R., Aghanim, N., et al. 2015, *A&A*, **576**, A106
- Planck Collaboration, X. I. I., Aghanim, N., Akrami, Y., et al. 2020, *A&A*, **641**, A12
- Planck Collaboration Int. XLVIII, Aghanim, N., Ashdown, M., et al. 2016, *A&A*, **596**, A109
- Press, W. H., Teukolsky, S. A., Vetterling, W. T., & Flannery, B. P. 1992, *Numerical Recipes in FORTRAN. The Art of Scientific Computing* (Cambridge: Cambridge Univ. Press)
- Purcell, C. R., Gaensler, B. M., Sun, X. H., et al. 2015, *ApJ*, **804**, 22
- Queiroz, A. B. A., Anders, F., Santiago, B. X., et al. 2018, *MNRAS*, **476**, 2556
- Ramírez, E. A., Magalhães, A. M., & Davidson 2017, *PASP*, **129**, 055001
- Riello, M., De Angeli, F., Evans, D. W., et al. 2021, *A&A*, **649**, A3
- Robin, A. C., Reylé, C., Derrière, S., & Picaud, S. 2003, *A&A*, **409**, 523
- Rodrigues, C. V., Magalhães, A. M., Coyne, G. V., & Piroola, S. J. V. 1997, *ApJ*, **485**, 618
- Rybizki, J., Green, G. M., Rix, H.-W., et al. 2022, *MNRAS*, **510**, 2597
- Savage, B. D., & Mathis, J. S. 1979, *ARA&A*, **17**, 73
- Schlafly, E. F., Meisner, A. M., Stutz, A. M., et al. 2016, *ApJ*, **821**, 78
- Serkowski, K., Mathewson, D. S., & Ford, V. L. 1975, *ApJ*, **196**, 261
- Simmons, J. F. L., & Stewart, B. G. 1985, *A&A*, **142**, 100
- Skolidis, R., Panopoulou, G. V., Tassis, K., et al. 2018, *A&A*, **616**, A52
- Skrutskie, M. F., Cutri, R. M., Stiening, R., et al. 2006, *AJ*, **131**, 1163
- Tassis, K., Ramaprakash, A. N., Readhead, A. C. S., et al. 2018, arXiv:1810.05652
- Taylor, M. B. 2005, in ASP Conf. Ser. 347, *Astronomical Data Analysis Software and Systems XIV*, ed. P. Shopbell, M. Britton, & R. Ebert (San Francisco, CA: ASP), 29
- Tody, D. 1986, *Proc. SPIE*, **627**, 733
- Tody, D. 1993, in ASP Conf. Ser. 52, *Astronomical Data Analysis Software and Systems II*, ed. R. J. Hanisch, R. J. V. Brissenden, & J. Barnes (San Francisco, CA: ASP), 173
- Vallée, J. P. 2015, *MNRAS*, **450**, 4277
- Vergely, J. L., Lallement, R., & Cox, N. L. J. 2022, *A&A*, **664**, A174
- Versteeg, M. J. F., Magalhães, A. M., Haverkorn, M., et al. 2023, *AJ*, **165**, 87
- Virtanen, P., Gommers, R., Oliphant, T. E., et al. 2020, *NatMe*, **17**, 261
- Wang, S., & Chen, X. 2019, *ApJ*, **877**, 116
- Whittet, D. C. B., Hough, J. H., Lazarian, A., & Hoang, T. 2008, *ApJ*, **674**, 304
- Wiegand, H. 1968, *Biometrische Zeitschrift*, **10**, 88